High-performance Fuel Cell Cathodes Exclusively Containing Atomically Dispersed Iron Active Sites

Hanguang Zhang,[a] Hoon T. Chung,[b] David A. Cullen,[c] Stephan Wagner,[d] Ulrike I. Kramm,[d] Karren L. More,[e] Piotr Zelenay,[b,*] and Gang Wu[a,*]

[a] Department of Chemical and Biological Engineering, University at Buffalo, The State University of New York, Buffalo, New York 14260, USA

[b] Materials Physics & Applications Division, Los Alamos National Laboratory, Los Alamos, New Mexico 87545, USA

[c] Materials Science and Technology Division, Oak Ridge National Laboratory, Oak Ridge, Tennessee 37831, USA

[d] Technische Universität Darmstadt, Department of Materials- and Earth Sciences and Department of Chemistry, 64287 Darmstadt, Germany

[e] Center for Nanophase Materials Sciences, Oak Ridge National Laboratory, Oak Ridge, Tennessee 37831, USA

Corresponding authors:

E-mail addresses: gangwu@buffalo.edu (G.W.) and zelenay@lanl.gov (P.Z.)

Abstract: Platinum group metal-free (PGM-free) catalysts for the oxygen reduction reaction (ORR) with atomically dispersed FeN_4 sites have emerged as a potential replacement for low-PGM catalysts in acidic polymer electrolyte fuel cells (PEFCs). In this work, we carefully tuned the doped Fe content in zeolitic imidazolate framework (ZIF)-8 precursors and achieved complete atomic dispersion of FeN_4 sites, the sole Fe species in the catalyst based on Mößbauer spectroscopy data. The Fe–N–C catalyst with the highest density of active sites achieved respectable ORR activity in rotating disk electrode (RDE) testing with a halfwave potential ($E_{½}$) of 0.88 ± 0.01 V *vs*. the reversible hydrogen electrode (RHE) in 0.5 M H_2SO_4 electrolyte. The activity degradation was found to be more significant when holding the potential at 0.85 V relative to standard potential cycling (0.6–1.0 V) in O_2 saturated acid electrolyte. The post-mortem electron microscopy analysis provides insights into possible catalyst degradation mechanisms associated with Fe–N coordination cleavage and carbon corrosion. High ORR activity was confirmed in fuel cell testing, which also divulged the promising performance of the catalysts at practical PEFC voltages. We conclude that the key factor behind the high ORR activity of the Fe–N–C catalyst is the optimum Fe content in the ZIF-8 precursor. While too little Fe in the precursors results in an insufficient density of FeN_4 sites, too much Fe leads to the formation of clusters and an ensuing significant loss in catalytic activity due to the loss of atomically dispersed Fe to inactive clusters or even nanoparticles. Advanced electron microscopy was used to obtain insights into the clustering of Fe atoms as a function of the doped Fe content. The Fe content in the precursor also affects other key catalyst properties such as the particle size, porosity, nitrogen-doping level, and carbon microstructure. Thanks to using model catalysts exclusively containing FeN_4 sites, it was possible to directly correlate the ORR activity with the density of FeN_4 species in the catalyst.

Introduction

The high cost and less than desirable performance of platinum group metal (PGM) catalysts for the oxygen reduction reaction (ORR) represent two big challenges facing acidic polymer electrolyte fuel cell (PEFC) technology. In this context, PGM-free catalysts emerge as an appealing alternative, provided they can fulfill the stringent activity and durability requirements of practical systems. Among various PGM-free catalysts developed to date, iron and nitrogen co-doped carbon catalysts (Fe-N-C) have shown encouraging activity and stability.(*1-3*) Spectroscopic studies and computational simulations suggest that FeN_4 and possibly similar species are the likely active sites for the ORR in such catalysts.(*4-6*) Increasing the density of FeN_4 sites by atomically dispersing Fe in the catalyst precursors appears to be an effective strategy for enhancing the catalytic activity.(*6-9*) Relative to other precursors, Zn-rich zeolitic imidazolate frameworks (ZIF-8) with the potential capability to host FeN_4 moieties as their key structural element are especially attractive for achieving high density of FeN_4 sites in catalysts obtained using a one-step high-temperature thermal activation approach.(*3, 9-19*) The synthesis of ZIF-8-derived catalysts typically does not require carbon-black supports and tedious post treatments such as acidic leaching and multiple heat treatments.(*20-23*) Nevertheless, the ORR activity of many ZIF-8-derived catalysts is often low in acidic media, likely due to an insufficient density of FeN_4 sites resulting from the loss of Fe to ORR-inactive metal-rich aggregates,(*24-26*) and poor control over the Fe dispersion in the catalysts. While the metal content in catalysts has been recognized as one of the critical factors affecting ORR performance of Fe-N-C catalysts,(*27-31*) little is known about the role of Fe during the active site formation and chemical forms of Fe involved in the ORR. The lack of well-defined Fe-N-C catalysts with homogeneous morphology and uniform active-site

dispersion has made rational design and fundamental knowledge gain in this area even more challenging.

In this work, we employed chemical doping to replace a small fraction of Zn ions in ZIF-8 precursors with Fe ions.(*20*) This approach allowed for precise control of the Fe content in the imidazolate precursors to study its effect on the catalytic properties and ORR activity. ZIFs have been identified as ideal precursors capable of providing imidazolate ligands to coordinate Fe sites in FeN_4 complexes within a 3D ZIF framework.(*25, 32, 33*) Thus, chemical doping of Fe into ZIF-8 allows better Fe dispersion in the precursor and precise control over the Fe content. Through subsequent high-temperature treatment, chemically Fe doped ZIFs are directly converted into high surface-area carbon, co-doped with Fe and N.(*20, 24, 34, 35*) Zn evaporation during the heat treatment benefits the formation of porous carbon phases, making active sites accessible during the ORR. By carefully tuning the doped Fe content, we synthesized model Fe-N-C catalysts with atomically dispersed and nitrogen coordinated FeN_4 sites uniformly dispersed in partially graphitized carbon phases, and without any formation of Fe-rich aggregates. Mößbauer spectroscopy verified the exclusive presence of Fe in the FeN_4 form. Advanced electron microscopy helped to monitor the Fe clustering process with an increase of the Fe doping content in the ZIF-8 precursors. The effect of the Fe content on the physical and catalytic properties was systematically studied. Catalysts with the highest FeN_4 density achieved a record ORR activity in acidic electrolytes, significantly minimizing the gap to the state of the art Pt/C catalysts. The atomically dispersed Fe catalysts were further studied in fuel cells, which showed promising performance and improvements in durability at practical operation voltages.

Results and Discussion

Atomic Fe site dispersion in catalysts

The Fe content in Fe-doped ZIF-8 (Fe-ZIF) was controlled by replacing part of the original Zn ions with Fe ions during the solution-phase synthesis of nanocrystalline ZIF-8 precursors in methanol The catalysts were labelled *x*Fe-ZIF, where *x* represents the atomic percent of Fe^{3+} relative to the total content of metal ions (Fe^{3+} and Zn^{2+}) in the ZIF-8 precursors in the range from 0.05 to 9.0 at.%. A single-step heat treatment at 1100 °C under an inert atmosphere flow was optimized to convert Fe-doped ZIF precursors directly into *x*Fe-ZIF catalysts without any additional post-treatments. Detailed synthesis procedures and extensive characterization methods are described in the Supporting Information. Fig. S1 shows the synthesis scheme.

The high angle annular dark field scanning transmission electron microscopy (HAADF-STEM) images in **Figures 1a-b** attest to the atomic and uniform dispersion of Fe atoms in the carbon phase. The two images shown, recorded for the same area on the best performing 1.5Fe-ZIF catalyst in the bright field and Z-contrast modes, respectively, are representative of the entire catalyst sample. Electron energy loss spectroscopy (EELS) revealed the tendency for the iron and nitrogen atoms to be co-located in the catalyst, directly suggesting coordination of Fe by N (**Figures 1c-d**). With an increase in the doped Fe content in the ZIF-8 precursors, the transition from atomically dispersed Fe sites to Fe clusters was observed (**Figures 1e-1h**). Clustering appeared in the catalyst derived from the precursor with 2.5 at% of Fe and became prevalent in the catalyst generated from the precursor with 3.0 at% of Fe (see the EELS data in the inset in Figure 1h). These ultra-high resolution STEM data confirm the key role of atomically dispersed Fe sites in the ORR. They also

explain the best activity of the 1.5Fe-ZIF catalyst due to the highest density of atomic Fe sites without any Fe clustering. A decrease in the ORR activity with a further increase in the Fe content is due to a gradual loss of atomically dispersed Fe to clusters and, ultimately, to Fe-rich nanoparticles.

Unlike in the earlier reported Fe-N-C catalysts having highly heterogeneous morphology,(*36*) the atomically dispersed catalyst with the optimum Fe content benefits from the conversion of all available Fe in the precursor to FeN_4 active sites, rather than to less active clusters or nanoparticles. The possible reason for the high Fe utilization in the catalyst is ligation of Fe atoms in the precursors by 2-methylimidazole and their spatial separation by Zn atoms within the ZIF-8 structure. The ligation of Fe atoms reduces their mobility and assures a uniform distribution throughout the precursor, also during the follow-up high-temperature treatment.(*37*) The spatial isolation prevents the formation of Fe-rich (Fe and/or Fe_3C) aggregates during the heat treatment. The coordination bonds between Zn^{2+} ions and 2-methylimidazole in the precursors are broken at around 500 ^oC, with zinc ions undergoing likely reduction to metallic Zn.(*13*) This leads to a reduction in microposity and surface area. Subsequent removal of metallic zinc species above 800 °C *via* evaporation gradually recovers the catalyst surface area, though not to the original level (**Figure S2**). When the Fe content in the precursor exceeds *ca.* 1.5 at.%, a fraction of Fe atoms, which can no longer be accommodated by the ZIF matrix, undergo agglomeration and ultimately conversion to Fe- and/or Fe_3C-rich clusters and nanoparticles during the high-temperature treatment. These forms of Fe do not contribute to the ORR activity in the acidic solution (at all or at a negligible level); on the contrary, their formation may cause a

decrease in the content of atomically dispersed Fe sites in the catalyst, probably due to the larger strength of Fe-Fe bonds than Fe-N bonds.

Our previous DFT and experimental X-ray absorption spectroscopy (XAS) studies suggest that FeN_4 is likely the active site in Fe-N-C catalysts.(*17, 38*) Highly iron-sensitive Mößbauer spectroscopy experiments were further carried out with the most active 1.5Fe-ZIF catalyst for more than 20 days to assure sufficient Fe signal. The result shown in **Figure 2a** indicates that the Mößbauer parameters of the doublets D1 and D2 are associated with Fe species in the FeN_4 configuration (**Figure 2c**). D2 is interpreted in terms of in-plane FeN_4 coordination integrated in graphene layers. D1 is accounted for by FeN_{2+2} coordination with pseudo-sixfold coordination of Fe by the four neighboring nitrogen atoms and carbon or nitrogen atoms in the axial direction from the graphene planes above and below (*cf*. the crystal structure of FePc).(*39, 40*) Our previous DFT calculations suggest that the FeN_4C_8 moiety should have higher intrinsic activity than the FeN_4C_{10} moiety.(*38*) Based on these results and previous correlation of activity vs. Mößbauer species,(*40*) D1 may act similarly to FeN_4C_8. It was predicted that the carbon atoms with dangling bonds adjacent to FeN_4 moieties are part of the ORR active sites, which bind the OOH intermediate to facilitate the cleavage of O-O bonds during the ORR. The Fe valence is close to 2+ in the catalysts, which is in good agreement with our previous XAS analysis suggesting a valence between 3+ and 2+.(*17*) It should be noted that the Fe catalysts were exposed to air before the analysis, causing possible oxidation. The valance can be changed depending on the applied potentials during the ORR. The uncertainty in the accurate determination of the Fe valence at the catalyst surface notwithstanding, the Mößbauer

results confirm the exclusive atomic dispersion of FeN_4 sites in the catalyst and the absence of any other Fe crystalline phases, such as metal, oxide, carbide, or nitride.

Since the coordination by four nitrogen atoms appears to stabilize atomically dispersed Fe sites in catalysts, nitrogen doping may be crucial to the ORR activity. N atoms can be doped at either the edge or bulk of the graphene planes as pyridinic and graphitic N with different binding energies of *ca.* 398.6 and 401.1 eV, respectively. We found that N doping is largely dependent on the content of doped Fe. The pyridinic nitrogen peak at 398.3 eV in the Fe-free ZIF sample is shifted positively to 398.7 eV in the Fe-ZIF catalysts (**Figure 2b**). This shift is likely attributed to an increase in the oxidation state of nitrogen due to the Fe-N bond formation. The best performing 1.5Fe-ZIF catalyst has the highest total and pyridinic nitrogen content of all the studied catalysts (**Figures 2d-2e**). This is related to the high concentration of FeN_4 sites, most likely involving pyridinic nitrogen atoms. The ratio of N to Fe in the 1.5Fe-ZIF catalyst is approximately 7:1, which is higher than the expected stoichiometric ratio of 4:1, indicating that a significant fraction of nitrogen in 1.5Fe-ZIF is not coordinated to Fe at all. Notably, the N content in catalysts tends to decrease with an increase in the Fe content above 1.5 at.%, implying a loss of N atoms from atomic Fe-N_4 sites as a result of Fe clustering at high Fe content.

Catalyst morphology and structure

To understand the effect of Fe doping in the precursor on the structure and morphology of the resulting Fe-N-C catalysts, we performed thorough characterization of the precursors and catalysts as a function of Fe content. The XRD patterns for the Fe-ZIF precursors were found to be independent of the Fe content (**Figure S3a**), indicating that Fe doping does not affect the ZIF crystallinity. After a single heat treatment at 1100 °C, the XRD patterns were

dominated by carbon peaks. The broad peak at 25° implies the presence of dominant amorphous carbon structures in all studied samples (**Figure S3b**). The 9.0Fe-ZIF catalyst contains a small amount of crystalline phases, likely Fe or/and Fe_3C particles.

The effect of the Fe content on the carbon structure was further studied using Raman spectroscopy (**Figure S4**). There is no significant differences between the "Fe-free" and 1.5Fe-ZIF catalysts. The similar values of I_D/I_G suggest that they have nearly identical carbon structures. However, an increase in the Fe content to 9.0 at.% results in a rise in the D and G bands, which have similar intensity (an I_D/I_G ratio of 1.0). Although the higher value of I_D/I_G in this case may indicate a carbon structure still rich in disordered phases, the narrowness of the D band and the appearance of the 2D band at 2700 cm^{-1} suggest an overall improvement of the carbon crystallinity.(*41*) These results point to an enhancement in the degree of graphitization in the 9.0Fe-ZIF catalyst. The subtle changes in the catalyst carbon structures were also studied using HR-TEM images (**Figure S5**). The micrographs are in good agreement with the Raman spectra, indicating an increase in the graphitization of the Fe-ZIF catalysts with higher Fe content in the precursors, linked to iron-catalyzed formation of graphene shells around the Fe or/and Fe_3C nanoparticles (**Figure S5**). The surface area and porosity of the Fe-doped precursors are nearly independent of the Fe content (**Figures S6** and **S7)**. All ZIF precursors show a similar BET surface area of around 1100 m^2/g. However, the high-temperature treatment, *e.g.*, at 1100 °C, leads to a significant reduction in the surface area of the catalysts to *ca.* 640 m^2/g for the 1.5Fe catalyst. This is mainly due to the loss of microporosity, evidenced by a decrease in the N_2 uptake at low pressures. An Fe content higher than 1.5 at.% results in a decrease in the catalyst surface

area due to less porous graphitic carbon catalyzed by metallic Fe clusters or nanoparticles.(*42*)

The effect of the Fe content on the size of the Fe-doped ZIF precursor nanocrystals was studied by scanning electron microscopy (SEM) (**Figure S8**). Fe doping leads to an increase in the ZIF crystal size from 40 nm, an average for the "Fe-free" ZIF-8, to 60 nm and 800 nm for ZIFs doped with 1.5 at.% and 9.0 at.% of Fe, respectively. In principle, crystal sizes are decided by the relative rates between seed nucleation and growth. The formation of larger particles can be explained by the nucleation rate of seeds becoming slower with an increase in the Fe content during the ZIF crystal formation, possibly because of the competition of Fe^{3+} ions with Zn^{2+} ions to coordinate 2-methylimidazole.(*43*) While the morphology of the Fe-doped ZIF precursors is retained in the catalysts, the "Fe-free" ZIF-8 precursor collapses during the high-temperature treatment, resulting in irregular particles and disordered carbon morphology with a low level of graphitization (**Figure S9)**. Consequently, Fe doping appears to be preventing the 3D ZIFs from collapsing during the heating treatment.

To elucidate the impact of Fe on the catalyst structure, we compared two catalysts derived from precursors with the optimum (1.5 at.%) and high (9.0 at.%) Fe content. As shown in **Figures 3** and **S10**, the catalyst derived from the ZIF precursor with 1.5 Fe at% maintains the polyhedron morphology, free of any metallic aggregates. The carbon phase in the 1.5Fe-ZIF catalyst is uniform, dominated by curved carbon fringes, characteristic of dominant amorphous carbon. In turn, the dominant morphological feature in the 9.0Fe-ZIF catalyst is much larger carbon particles. The carbon polyhedrons are on a *ca*. 1000 nm scale and tend to fuse together, a shape in contrast with smaller, isolated polyhedron particles in the 1.5Fe-ZIF catalyst. The catalyst derived from the

9.0 at.% Fe precursor also contains numerous metallic aggregates, protected by several layers of highly graphitized carbon shells (**Figure S5**). This feature is often observed with the early Fe-N-C catalysts.(*44*) In general, highly graphitized Fe-based catalysts are less ORR active in acidic environments, possibly due to the very low content of defects needed for hosting the FeN_4 sites.(*20*)

Catalyst performance

The ORR activity of the catalysts derived from Fe-doped ZIF precursors with Fe content ranging from 0 to 9.0 at.% was evaluated using the rotating ring disk electrode (RRDE) in O_2-saturated 0.5 M H_2SO_4 electrolyte at 900 rpm and 25 °C (**Figures 4** and **S10**-**S12**). Initially, the activity increased continuously with an increase in Fe content in precursors from 0 to 1.5 at.%. The performance of the "Fe-free" sample was found to be very poor, as indicated by E_{onset} of 0.82 V and $E_{½}$ of 0.60 V. An addition of even small amount of Fe (0.05 at.%) to the precursor resulted in a significant increase in the ORR activity, with E_{onset} and $E_{½}$ rising to 0.92 V and 0.77 V, respectively. Such a dramatic increase in the ORR activity highlights the key role of Fe.(*45, 46*) A gradual increase in the Fe content in the precursor to 0.5 at.% led to a positive shift in $E_{½}$ to 0.81 V. When the Fe content in precursors was increased to 1.5 at.% Fe, the $E_{½}$ of the resulting catalyst reached the value of 0.87 ± 0.01 V, indicating dramatically increased density of active sites, likely associated with Fe content in precursors. This RDE performance is similar to that of Pt/C catalysts (*e.g.*, E_{onset} = 1.0 V, $E_{½}$= 0.88 V, 60 $\mu g_{Pt}/cm^2$)(*47*). However, further increase in the Fe precursor content, up to 2.5 at.%, resulted in a drop in the $E_{½}$ value to 0.85 V. Even more substantial activity loss was observed with the 3.0Fe-ZIF catalyst ($E_{½}$ of 0.82 V), possibly reflecting a reduction in the active site density due to the formation of Fe or/and FeC_3

particles. This downward trend in the activity continued with further increase in the Fe content, up to the highest studied Fe content value of 9.0 at.%. Since the change in Fe content in the precursor from 1.5 to 2.5 at.% was found to significantly affect ORR activity of Fe-ZIF catalysts, a more precise optimization of the Fe content was performed in a narrow range between 1.2 to 2.5 at.% (**Figure S11d**). The highest ORR activity was measured with catalysts derived from precursors containing between 1.5-1.8 at.% of Fe. This content corresponds to the top of a volcano curve describing the dependence of the ORR activity on the Fe content in the ZIF-8 precursors. The continuous increase in the ORR activity with an increase in the Fe content of the ZIF-8 precursors from 0 to 1.5 at.% attests to the dependence of the ORR activity on the number of FeN_4 sites. Once the Fe content in the precursors reaches a certain threshold, clustering of single atomic Fe sites occurs during the heating treatment, which significantly reduces the number of FeN_4 active sites. This observation can serve as guidance for designing advanced Fe-N-C catalysts targeting a higher content of atomically dispersed Fe for ORR activity enhancement. The desnity of FeN_4 active sites in the best performing 1.5Fe-ZIF catalyst was also approximately estimated using a method developed by Sahraie et al.(*6*) The maximum mass-based site density (MSD_{max}) are found to be 1.3×10^{20} (site g_{cat}^{-1}) and 2.1 (e s^{-1} $site^{-1}$), respectively. They are some of the highest values of MSD_{max} and TOF reported to date for PGM-free catalysts (**Table S2**).

The electrochemically accessible surface area (ECSA) was estimated from the double layer capacitance as determined using cyclic voltammetry (CV) in N_2 saturated 0.5 M H_2SO_4 electrolyte.(*49*) It should be noted that the ECSAs of catalysts are often lower than the corresponding BET surface areas measured by N_2 isothermal absorption/desorption.

The possible reason for the observed difference between ECSAs and BET surface areas is the presence of ultra-small micropores in catalysts, which are accessible to N_2 molecules in the gas adsorption studies, but not to H_2O in an aqueous electrolyte. Bothe the ECSA and BET surface area values differ with an increase in Fe content (**Figure S12** and **Table S3**). This reduced surface area of the catalysts combined with the loss of FeN_4 sites due to clustering likely further accelerates the activity decline of catalysts with high Fe content.

The values of the H_2O_2 yield as a function of Fe content in the precursor were determined in RRDE experiments (**Figure 4b**). The highest H_2O_2 yield was measured with the catalyst synthesized from a Fe-free ZIF precursor (15-20%). Peroxide yields were significantly lower for the catalysts synthesized using Fe-doped ZIF precursors, reaching values below 1% for the 1.5Fe-ZIF catalyst at a loading of 0.8 mg cm^{-2} (error bars provided in **Figure S11**). This result points to a significant contribution of the four-electron path in the ORR and/or to an increase in the rate of the 2e+2e process. However, the catalysts with higher Fe content, the 9.0Fe-ZIF catalyst in particular, generated relatively high H_2O_2 yields of 3-4% during the ORR.

The best performing 1.5Fe-ZIF catalyst was used for fabricating membrane electrode assemblies (MEAs) studied in fuel cells in both O_2 and air. The purpose of studying the fuel cell performance in O_2 (1.0 bar partial pressure) was to minimize mass-transport losses when determining the catalyst activity in MEAs (**Figure 4c**). The open cell voltage (OCV) measured with an MEA was 0.98 V, in good agreement with RDE tests in acidic electrolytes, only *ca*. 20 mV lower than the value measured with a Pt/C cathode (0.2 mg_{Pt}/cm^2) under the same conditions.(*36*) A current density of 0.044 A/cm^2 was achieved at 0.87 V (*iR*-free), only 30 mV away from U.S. DOE activity target (0.90 V). The current

density generated at a reference fuel cell voltage of 0.80 V was 145 mA/cm^2, which is more than double the current density measured previously with a Fe-N-C catalyst derived from polyaniline in 2011 (~70 mA/cm^2, at a much higher O_2 partial pressure of 2.3 bar).(*44*) This result shows that the higher ORR activity measured in aqueous electrolytes can be realized in a polymer electrolyte fuel cell cathode. An MEA with the 1.5Fe-ZIF catalyst in the cathode was also studied under air at a total partial pressure of of 1.0 bar (O_2 partial pressure of *ca.* 0.2 bar). The OCV value decreased by only 30 mV relative to that measured in O_2, from 0.98 V to 0.95 V, and the current density at 0.80 V dropped by nearly 50%, from 145 to 75 mA/cm^2 (**Figure 4d**), typical of oxygen- and air-operated cathodes. The H_2-air performance in this work with a peak powder density of 360 mW/cm$_2$ is still one of the highest reported to date for PGM-free catalysts (**Table S4**).(*1, 44*).

Stability of Fe-N-C cathode catalysts in acidic media represents a major challenge, especially at high potentials (>0.6 V). According to the U.S. DOE, dynamic voltage cycling between 0.6 and 1.0 V or holding the voltage at a constant value is more relevant to real fuel cell operation. In this work, we employed two stability testing protocols, including potential cycling and holding a constant potential/voltage to evaluate the durability of the atomically dispersed Fe-N-C catalysts. 40,000 accelerated stress test (AST) potential cycles (0.6-1.0 V) in O_2 saturated 0.5 M H_2SO_4 electrolyte led to only a 30 mV loss in the $E_{½}$ value (**Figure 5a**), attesting to much improved catalyst stability compared to that of an earlier Fe-N-C catalyst, which lost 80 mV after only 5000 cycles.(*50*) The post-mortem microscopy analysis indicates that atomically dispersed and nitrogen-coordinated Fe sites are still clearly visible in the 1.5Fe-ZIF catalyst after the AST test (**Figures 5b-c** and **S13**), attesting to very good stability of a majority of FeN_4 sites during the dynamic potential

cycling test. The morphology of the carbon particles remained intact, with nearly identical sizes and clear edges of polyhedral particles compared to the catalysts before the AST (**Figure S14**), suggesting insignificant carbon corrosion.

We also conducted constant-potential testing of the catalyst by holding the potential at a relatively high potential of 0.85 V in O_2 saturated 0.5 M H_2SO_4 for 100 hours (**Figure 5d**). We recorded ORR polarization plots every 10 hours, finding that the ORR activity partially recovered every time a polarization plot was recorded in the range from 0 to 1.0 V. The reversible degradation probably is due to the surface functionalization of carbon atoms adjacent to the FeN_4 sites. However, the rate of unrecoverable degradation remained unchanged throughout the test likely resulting from possible demetallization. In the end, the catalyst suffered from a significant decrease in the ORR activity, especially in the first 20 hours, when approximately half of the initial ORR activity was lost. At the end of the 100-hour test, the remaining activity was only 30% of that measured initially. The HAADF-STEM images indicate severe carbon corrosion, with catalyst particles becoming rounded and agglomerated (**Figure S15**).

While a majority of atomically dispersed sites are still present after the durability test, these Fe atoms in those clusters appear no longer coordinated by nitrogen (**Figures 5e-f**). Because Fe and N EELS signals cannot be detected simultaneously at the atomic level. Also, some iron clusters become apparent. The possible degradation mechanisms involve the cleavage of Fe-N coordination likely due to Fe oxidation and carbon corrosion in the catalyst. Carbon corrosion may also be responsible for the loss of Fe-N coordination due to weakening of the Fe-N and N-C bonds, ultimately resulting in decomposition of FeN_4 sites.(*51,52*) If independently confirmed, these degradation mechanisms set a possible path

towards stabilizing Fe-N-C catalysts *via* making the carbon structure more robust and corrosion-resistant, especially next to the active site(s).

Finally, the life tests of MEAs were performed in H_2-air fuel cells at constant voltages of 0.55 V and 0.70 V for approximately 100 hours **(Figure 5g)**. While the performance degrades at both voltages, the tests reveal, perhaps for the first time, that atomically dispersed Fe catalysts can sustain respectable current densities at practically relevant voltages for prolonged times. Fuel cell polarization plots recorded at different times during the life test at 0.70 V are shown in **Figure 5h**. They indicate similar performance losses across the entire range of fuel cell voltages. The current density loss at 0.80 V is *ca.* 30 mA/cm^2 after the first 23 hours, but much less later on (35 mA/cm^2 after 42 hours and 46 mA/cm^2 at the end of the 118-hour test). Similarly, at a low voltage of 0.40 V, the total loss in current density during the test is 35%, with most of it happening in the first 23 hours.

Compared to aqueous acidic electrolytes, performance degradation in fuel cell MEAs is much more complex with several mechanisms possible.(*53*) In addition to catalyst degradation due to demetalation and carbon corrosion, degradation of three-phase (gas, liquid, solid) interfaces and water flooding in micropores may lead to severe proton and mass transfer resistances. It should be noted that, unlike in aqueous electrolytes, the confined H_2O_2 formation within the fuel cell cathode could be more harmful than in an aqueous electrolyte, resulting in free radicals known to cause active site degradation and carbon corrosion.(*53*) In this study, the performance degradation of the Fe–N–C catalyst in MEAs was found to be comparable at 0.55 V and 0.70 V (ca. 45–50% current loss). However, the causes of performance loss could be different in these two cases. At a lower voltage of 0.55 V, the catalyst degradation may be due to a relatively high amount of generated H_2O_2, resulting in a higher yield of hydroperoxyl than at 0.70 V, known to be highly detrimental

to both the ionomer and carbon. At a higher voltage of 0.70 V, the performance loss is more likely to be caused by accelerated carbon corrosion and the ensuing deterioration of the carbon matrix hosting FeN_4 sites. Further studies under various operating conditions are necessary to identify the causes of the PGM-free cathode degradation and address the stability challenge before the PGM-free catalysts become viable for PEFC applications.

Conclusions

FeN_4 sites have been considered the most likely ORR active sites in PGM-free catalysts in acidic media. In this work, we employed a chemical doping method for precisely controlling the Fe content in ZIF-8 precursors (from 0 to 9 at%). Through fine-tuning and optimizing the Fe content to 1.5 at.%, we obtained a catalyst with fully atomically dispersed and nitrogen-coordinated FeN_4 sites, free of any metal-rich clusters and nanoparticles. This catalyst with the highest density of active sites yields the best ORR activity. A higher than optimum Fe content in the precursor results in the formation of clusters and nanoparticles that "consume" Fe atoms, reducing the number of active sites in the catalyst. The volcano-like dependence between the ORR activity and Fe content provides an insight into the role of Fe in Fe-N-C ORR catalysts. Using these model catalysts with controlled Fe content, we also described the effect of the Fe in the precursors on the catalyst morphologies and structures, such as on the particle size, porosity, nitrogen-doping level, and carbon microstructure. The excess Fe negatively impacts the catalyst performance. In particular, high Fe content leads to larger catalyst particles, and reduced surface area, and pore volume. The Fe clusters and nanoparticles also catalyze carbon graphitization, limiting the number of carbon defects as hosts for active sites.

The highly dispersed FeN_4 sites in the catalysts appear to be directly responsible for the record-high ORR activity of the PGM-free catalysts in RDE testing and in a fuel cell cathode. Stability studies by potential cycling(0.6-1.0 V) and at a constant high potential of 0.85 V, along with post-mortem microscopy, suggest that the loss of Fe-N coordination and significant carbon corrosion are responsible for the ORR activity decrease in acidic aqueous electrolytes. Although the durability of the catalyst with atomically dispersed FeN_4 sites at a practically relevant voltage 0.70 V is encouraging, the stability challenges need to be overcome before the PGM-free catalysts become viable for fuel cell applications.

Methods

Catalyst synthesis. Fe content is given in this work in terms of atomic percent of Fe versus the total metal (Fe+Zn) content in the catalyst precursor. The synthesis of 1.5Fe-ZIF catalyst, *i.e.*, the catalyst derived from precursor with 1.5 at.% Fe content, is given here as an example: Zinc nitrate hexahydrate (3.39 g) and iron nitrate nonahydrate (85 mg) were dissolved in 500 mL methanol in a round-bottom flask, followed by addition of 500 mL methanol solution of 2-methylimidazole (3.94 g). The obtained mixture were then kept at 60 °C for 24 h. The resulting suspension was separated by centrifuging at 8700 rpm to collect the precipitants, then washed with ethanol three times. The thus obtained catalyst precursor was dried at 60 °C in a vacuum oven for 8 h, before being heat-treated in a tube furnace at 1100 °C under N_2 for 1 h to obtain final catalyst (1.5Fe-ZIF in this example).

Material characterization. Atomic-resolution micrographs were obtained using a Nion UltraSTEM U100 microscope operated at 60 keV and equipped with a Gatan Enfina electron energy loss spectrometer (EELS). Bright field (BF) and high-angle annular dark-field (HAADF)

micrographs were recorded in image pairs. EEL spectra to confirm the composition of Fe sites and clusters were obtained after eliminating data noise using the open source Hyperspy python library. Catalyst morphology was also studied using scanning electron microscopy (SEM) on a Hitachi SU 70 microscope operating at 5 kV. The crystal phases in the samples were identified using powder X-ray diffraction (XRD) on a Rigaku Ultima IV diffractometer with Cu K-α X-rays. X-ray photoelectron spectroscopy (XPS) was performed using a Kratos AXIS Ultra DLD XPS system equipped with a hemispherical energy analyzer and a monochromatic Al Kα source. The elemental Fe content in precursors was determined by inductively coupled plasma (ICP), following complete digestion of precursors in 65% nitric acid. The N_2 isothermal adsorption/desorption was recorded at 77 K using a Micromeritics TriStar II BET instrument. Samples were degassed at 150 °C for 5 h under vacuum prior to nitrogen physisorption measurements. Mößbauer spectroscopy was performed in transmission mode at room temperature using a Co^{57}/Rh source. Data were collected with a scintillation detector and calibration of the velocity axis was made with respect to α–Fe foil.

Electrochemical measurements. All electrochemical measurements were performed using a CHI Electrochemical Station (Model 760b) in a conventional three-electrode cell at room temperature. A glassy carbon rotating disk electrode (GC-RDE) was used as the working electrode. Each catalyst was mixed with isopropanol and 5 wt% suspension of Nafion® in alcohols to produce catalyst ink that was drop-cast onto the GC-RDE and air-dried at 60 °C. Cyclic voltammetry (CV) was then recorded in N_2-saturated 0.5 M H_2SO_4 electrolyte at a scan rate of 20 mV/s to estimate the electrochemically accessible surface area from the double layer capacitance, assuming a capacitance 30 μF per cm^2 of the catalyst surface. (M-N-C catalysts contain no less than 95% of carbon.) The ORR activity and four-electron selectivity were determined from rotating ring disc electrode (RRDE) measurements, performed in O_2-saturated 0.5 M H_2SO_4 at room temperature

and rotation rate of 900 rpm. A graphite rod was used as the counter electrode. $Hg/HgSO_4$ in saturated K_2SO_4, was the reference electrode. The catalyst loading RDE/RRDE testing was 0.8 mg/cm^2, except in the loading dependence studies. ORR steady-state polarization plots were recorded using potential steps of 0.05 V at time intervals of 30 s in the potential range from 1.0 to 0 V *vs*. RHE.

Fuel cell testing. Catalyst ink containing 35 wt% of Nafion® was made by ultrasonically mixing the catalyst, isopropanol, de-ionized water, and 5% Nafion® suspension in alcohols at a 1:12:12:11 weight ratio for three hours. The inks were applied to the membrane by brushing until the cathode catalyst loading of ~4.0 mg cm^{-2} was reached. A commercial Pt-catalyzed gas diffusion electrode (GDE, 0.2 mg_{Pt}/cm^2, IRD Fuel Cells) was used at the anode. The cathode gas diffusion layer and the anode GDE were hot-pressed onto a Nafion® 212 membrane at 125°C for 5 minutes. The geometric surface area of the membrane electrode assembly (MEA) was 5.0 cm^2. Fuel cell testing was carried out in a single-cell fuel cell with a single-serpentine flow channels. Pure hydrogen and air/oxygen humidified at 80 °C were supplied to the anode and cathode, respectively, at a flow rate of 200 mL/min. The total partial pressure of gases at both electrodes was 1.0 bar. Fuel cell polarization plots were recorded using standard fuel cell test stations (Fuel Cell Technologies Inc.) in a voltage control mode.

Acknowledgements

This work was financially supported with start-up funding from the University at Buffalo, SUNY. Materials synthesis and characterization effort was also supported by National Science Foundation (CBET-1604392). Financial support from the DOE-EERE Fuel Cell Technologies Office is also gratefully acknowledged. We thank Dr. Ye Lin for XPS data analysis. A portion of the electron microscopy research was conducted in the Center for

Nanophase Materials Sciences of Oak Ridge National Laboratory, which is a DOE Office of Science User Facility. U.I.K. and S.W. would like to acknowledge financial support by German Research Foundation (GSC1070) and the Federal Ministry of Education and Research (05K16RD1).

Author Contributions

G.W. and P.Z. designed experiments, analyzed the experimental data, and wrote the manuscript. H.Z. synthesized catalyst samples and carried out electrochemical measurements. H.T.C. performed fuel cell tests. D.A.C. and K.L.M. carried out electron microscopy analysis. U.I.K. and S.W. conducted Mößbauer spectroscopy experiments.

References and Notes

1. H. T. Chung *et al.*, Direct atomic-level insight into the active sites of a high-performance PGM-free ORR catalyst. *Science* **357**, 479-484 (2017).
2. M. Shao, Q. Chang, J.-P. Dodelet, R. Chenitz, Recent advances in electrocatalysts for oxygen reduction reaction. *Chem. Rev* **116**, 3594-3657 (2016).
3. A. Zitolo *et al.*, Identification of catalytic sites for oxygen reduction in iron- and nitrogen-doped graphene materials. *Nat. Mater.* **14**, 937-942 (2015).
4. S. Kattel, G. Wang, Reaction pathway for oxygen reduction on FeN4 embedded graphene. *The journal of physical chemistry letters* **5**, 452-456 (2014).
5. E. F. Holby, G. Wu, P. Zelenay, C. D. Taylor, Structure of Fe–N x–C Defects in Oxygen Reduction Reaction Catalysts from First-Principles Modeling. *The Journal of Physical Chemistry C* **118**, 14388-14393 (2014).

6. N. R. Sahraie *et al.*, Quantifying the density and utilization of active sites in non-precious metal oxygen electroreduction catalysts. *Nature Communications* **6**, 8618 (2015).

7. G. Wu *et al.*, Carbon nanocomposite catalysts for oxygen reduction and evolution reactions: From nitrogen doping to transition-metal addition. *Nano Energy* **29**, 83-110 (2016).

8. Z. Qiao *et al.*, 3D polymer hydrogel for high-performance atomic iron-rich catalysts for oxygen reduction in acidic media. *Applied Catalysis B: Environmental* **219**, 629-639 (2017).

9. Y. Chen *et al.*, Isolated Single Iron Atoms Anchored on N-Doped Porous Carbon as an Efficient Electrocatalyst for the Oxygen Reduction Reaction (Angew. Chem. Int. Ed. 24/2017). *Angewandte Chemie International Edition* **56**, 7003-7003 (2017).

10. H. Zhang, H. Osgood, X. Xie, Y. Shao, G. Wu, Engineering nanostructures of PGM-free oxygen-reduction catalysts using metal-organic frameworks. *Nano Energy* **31**, 331-350 (2017).

11. J. Guo, Y. Li, Y. Cheng, L. Dai, Z. Xiang, Highly Efficient Oxygen Reduction Reaction Electrocatalysts Synthesized under Nanospace Confinement of Metal–Organic Framework. *ACS Nano* **11**, 8379-8386 (2017).

12. H. M. Barkholtz, D.-J. Liu, Advancements in rationally designed PGM-free fuel cell catalysts derived from metal–organic frameworks. *Materials Horizons* **4**, 20-37 (2017).

13. E. Proietti *et al.*, Iron-based cathode catalyst with enhanced power density in polymer electrolyte membrane fuel cells. *Nat Commun* **2**, 416 (2011).

14. W. Xia *et al.*, Well-defined carbon polyhedrons prepared from nano metal-organic frameworks for oxygen reduction. *Journal of Materials Chemistry A* **2**, 11606-11613 (2014).

15. D. Zhao *et al.*, Highly Efficient Non-Precious Metal Electrocatalysts Prepared from One-Pot Synthesized Zeolitic Imidazolate Frameworks. *Advanced Materials* **26**, 1093-1097 (2014).

16. P. Yin *et al.*, Single Cobalt Atoms with Precise N-Coordination as Superior Oxygen Reduction Reaction Catalysts. *Angewandte Chemie International Edition* **55**, 10800-10805 (2016).

17. H. Zhang *et al.*, Single Atomic Iron Catalysts for Oxygen Reduction in Acidic Media: Particle Size Control and Thermal Activation. *Journal of the American Chemical Society*, (2017).

18. H. Zhang, J. Nai, L. Yu, X. W. D. Lou, Metal-Organic-Framework-Based Materials as Platforms for Renewable Energy and Environmental Applications. *Joule* **1**, 77-107 (2017).

19. B. Y. Xia *et al.*, A metal–organic framework-derived bifunctional oxygen electrocatalyst. *Nature Energy* **1**, 15006 (2016).

20. X. Wang *et al.*, Directly converting Fe-doped metal–organic frameworks into highly active and stable Fe-N-C catalysts for oxygen reduction in acid. *Nano Energy* **25**, 110-119 (2016).

21. J. Li *et al.*, Atomically dispersed manganese catalysts for oxygen reduction in proton-exchange membrane fuel cells. *Nature Catalysis* **1**, 935-945 (2018).

22. Y. He *et al.*, Highly active atomically dispersed CoN4 fuel cell cathode catalysts derived from surfactant-assisted MOFs: carbon-shell confinement strategy. *Energy & Environmental Science*, doi: 10.1039/C1038EE02694G (2019).

23. X. X. Wang *et al.*, Nitrogen-Coordinated Single Cobalt Atom Catalysts for Oxygen Reduction in Proton Exchange Membrane Fuel Cells. *Advanced Materials* **30**, 1706758 (2018).

24. P. Su *et al.*, Nitrogen-doped carbon nanotubes derived from Zn-Fe-ZIF nanospheres and their application as efficient oxygen reduction electrocatalysts with in situ generated iron species. *Chemical Science* **4**, 2941-2946 (2013).

25. T. Liu *et al.*, An Fe-N-C hybrid electrocatalyst derived from a bimetal-organic framework for efficient oxygen reduction. *Journal of Materials Chemistry A* **4**, 11357-11364 (2016).

26. S. Zhao *et al.*, Carbonized Nanoscale Metal–Organic Frameworks as High Performance Electrocatalyst for Oxygen Reduction Reaction. *ACS nano* **8**, 12660-12668 (2014).

27. L. Zhang, K. Lee, C. W. B. Bezerra, J. Zhang, J. Zhang, Fe loading of a carbon-supported Fe–N electrocatalyst and its effect on the oxygen reduction reaction. *Electrochimica Acta* **54**, 6631-6636 (2009).

28. F. Jaouen, S. Marcotte, J.-P. Dodelet, G. Lindbergh, Oxygen Reduction Catalysts for Polymer Electrolyte Fuel Cells from the Pyrolysis of Iron Acetate Adsorbed on Various Carbon Supports. *The Journal of Physical Chemistry B* **107**, 1376-1386 (2003).

29. M. Lefèvre, J. P. Dodelet, P. Bertrand, Molecular Oxygen Reduction in PEM Fuel Cells: Evidence for the Simultaneous Presence of Two Active Sites in Fe-Based Catalysts. *The Journal of Physical Chemistry B* **106**, 8705-8713 (2002).

30. S. Li *et al.*, Heat-treated cobalt–tripyridyl triazine (Co–TPTZ) electrocatalysts for oxygen reduction reaction in acidic medium. *Electrochimica Acta* **55**, 4403-4411 (2010).

31. X. Wang *et al.*, An efficient Co-N-C oxygen reduction catalyst with highly dispersed Co sites derived from a ZnCo bimetallic zeolitic imidazolate framework. *RSC Advances* **6**, 37965-37973 (2016).

32. L. Shang *et al.*, Well-Dispersed ZIF-Derived Co,N-Co-doped Carbon Nanoframes through Mesoporous-Silica-Protected Calcination as Efficient Oxygen Reduction Electrocatalysts. *Advanced Materials* **28**, 1668-1674 (2016).

33. V. Armel *et al.*, Structural Descriptors of Zeolitic–Imidazolate Frameworks Are Keys to the Activity of Fe–N–C Catalysts. *Journal of the American Chemical Society* **139**, 453-464 (2017).

34. B. You *et al.*, Bimetal-Organic Framework Self-Adjusted Synthesis of Support-Free Nonprecious Electrocatalysts for Efficient Oxygen Reduction. *Acs Catalysis* **5**, 7068-7076 (2015).

35. V. Ordomsky, B. Legras, K. Cheng, S. Paul, A. Khodakov, The role of carbon atoms of supported iron carbides in Fischer–Tropsch synthesis. *Catalysis Science & Technology* **5**, 1433-1437 (2015).

36. G. Wu, P. Zelenay, Nanostructured nonprecious metal catalysts for oxygen reduction reaction. *Accounts of chemical research* **46**, 1878-1889 (2013).

37. X. J. Wang *et al.*, MOF derived catalysts for electrochemical oxygen reduction. *Journal of Materials Chemistry A* **2**, 14064-14070 (2014).

38. K. Liu, G. Wu, G. Wang, Role of Local Carbon Structure Surrounding FeN4 Sites in Boosting the Catalytic Activity for Oxygen Reduction. *The Journal of Physical Chemistry C* **121**, 11319-11324 (2017).

39. U. I. Koslowski, I. Abs-Wurmbach, S. Fiechter, P. Bogdanoff, Nature of the catalytic centers of porphyrin-based electrocatalysts for the ORR: a correlation of kinetic current density with the site density of Fe− N4 centers. *The Journal of Physical Chemistry C* **112**, 15356-15366 (2008).

40. U. I. Kramm *et al.*, Structure of the catalytic sites in Fe/N/C-catalysts for O 2-reduction in PEM fuel cells. *Physical Chemistry Chemical Physics* **14**, 11673-11688 (2012).

41. M. Pawlyta, J.-N. Rouzaud, S. Duber, Raman microspectroscopy characterization of carbon blacks: Spectral analysis and structural information. *Carbon* **84**, 479-490 (2015).

42. V. Nallathambi, J.-W. Lee, S. P. Kumaraguru, G. Wu, B. N. Popov, Development of high performance carbon composite catalyst for oxygen reduction reaction in PEM Proton Exchange Membrane fuel cells. *Journal of Power Sources* **183**, 34-42 (2008).

43. J. K. Zaręba, M. Nyk, M. Samoć, Co/ZIF-8 Heterometallic Nanoparticles: Control of Nanocrystal Size and Properties by a Mixed-Metal Approach. *Crystal Growth & Design* **16**, 6419-6425 (2016).

44. G. Wu, K. L. More, C. M. Johnston, P. Zelenay, High-performance electrocatalysts for oxygen reduction derived from polyaniline, iron, and cobalt. *Science* **332**, 443-447 (2011).

45. E. F. Holby, G. Wu, P. Zelenay, C. D. Taylor, Structure of Fe-Nx-C Defects in Oxygen Reduction Reaction Catalysts from First Principles Modeling. *J. Phys. Chem. C* **118**, 14388–14393 (2014).

46. S. Kattel, G. Wang, A density functional theory study of oxygen reduction reaction on Me–N 4 (Me= Fe, Co, or Ni) clusters between graphitic pores. *Journal of Materials Chemistry A* **1**, 10790-10797 (2013).

47. C. Chen *et al.*, Highly Crystalline Multimetallic Nanoframes with Three-Dimensional Electrocatalytic Surfaces. *Science* **343**, 1339-1343 (2014).

48. X. Wang, Q. Li, H. Pan, Y. Lin, Y. Ke, H. Sheng, M. T. Swihart and G. Wu, *Nanoscale* **7**, 20290–20298 (2015).

49. G.Wu,M. A. Nelson,N.H.Mack, S. Ma, P. Sekhar, F. H.Garzon and P. Zelenay, *Chem. Commun.* **46**, 7489–7491 (2010).

50. U. I. Kramm, M. Lefe`vre, P. Bogdanoff, D. Schmeiser and J.-P. Dodelet, *J. Phys. Chem. Lett.* **5**, 3750–3756 (2014).

51. V. Goellner, C. Baldizzone, A. Schuppert, M. T. Sougrati, K. Mayrhofer and F. Jaouen, *Phys. Chem. Chem. Phys.* **16**, 18454–18462 (2014).

52. X. X. Wang, V. Prabhakaran, Y. He, Y. Shao and G. Wu, *Adv. Mater.* **31**, 1805126 (2019).

Graphitic Abstract:

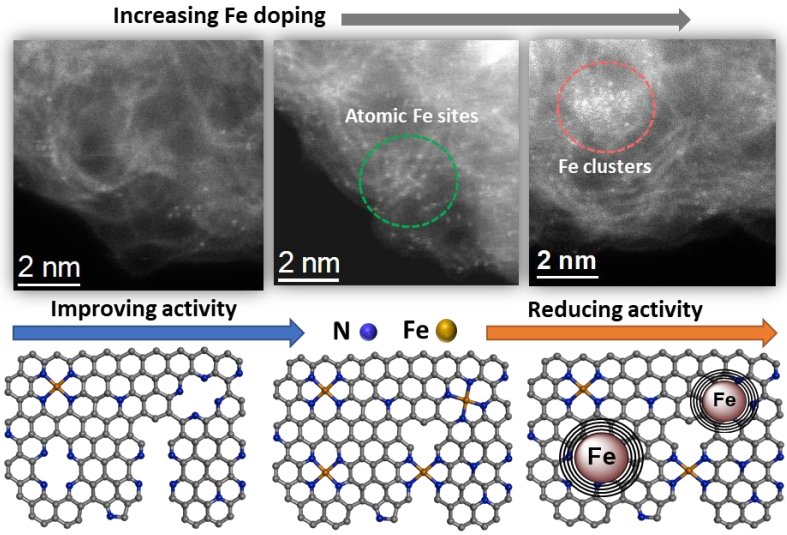

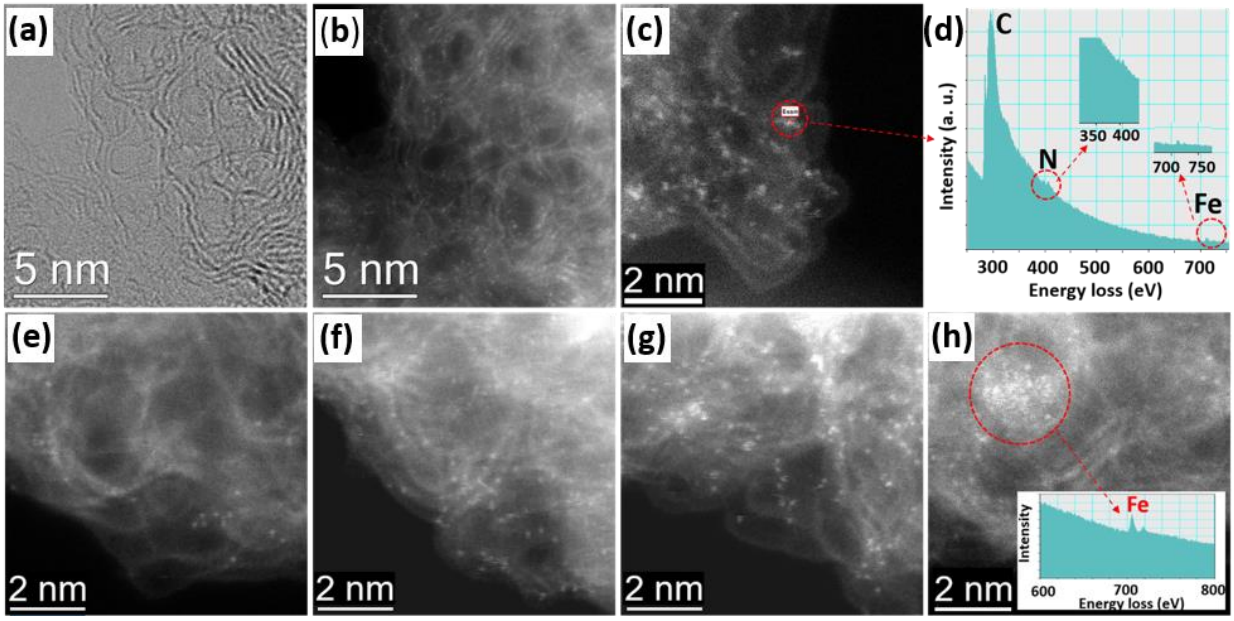

Figure 1. Atomic dispersion of Fe sites in Fe-doped ZIF catalysts. (a) Bright-field STEM image showing partially graphitized carbon fringes in the best performing 1.5Fe-ZIF catalyst; (b) HAADF-STEM image of the same depicting the single Fe sites (bright dots) dispersed throughout the carbon phase in the 1.5Fe-ZIF catalyst; (c-d) Fe-N-C structure analyzed by HAADF-STEM and EELS, respectively; (e-h) evolution of atomically dispersed Fe sites to Fe-rich aggregates with an increase in iron content in ZIF precursors with 0.05Fe-ZIF (e), 1.5Fe-ZIF, 2.5Fe-ZIF (g) and 3.0Fe-ZIF (h). (Fe clusters beginning to form in catalyst derived from Fe-ZIF precursor 2.5 at.% of Fe); EELS confirmation of cluster formation shown in the inset in (h).

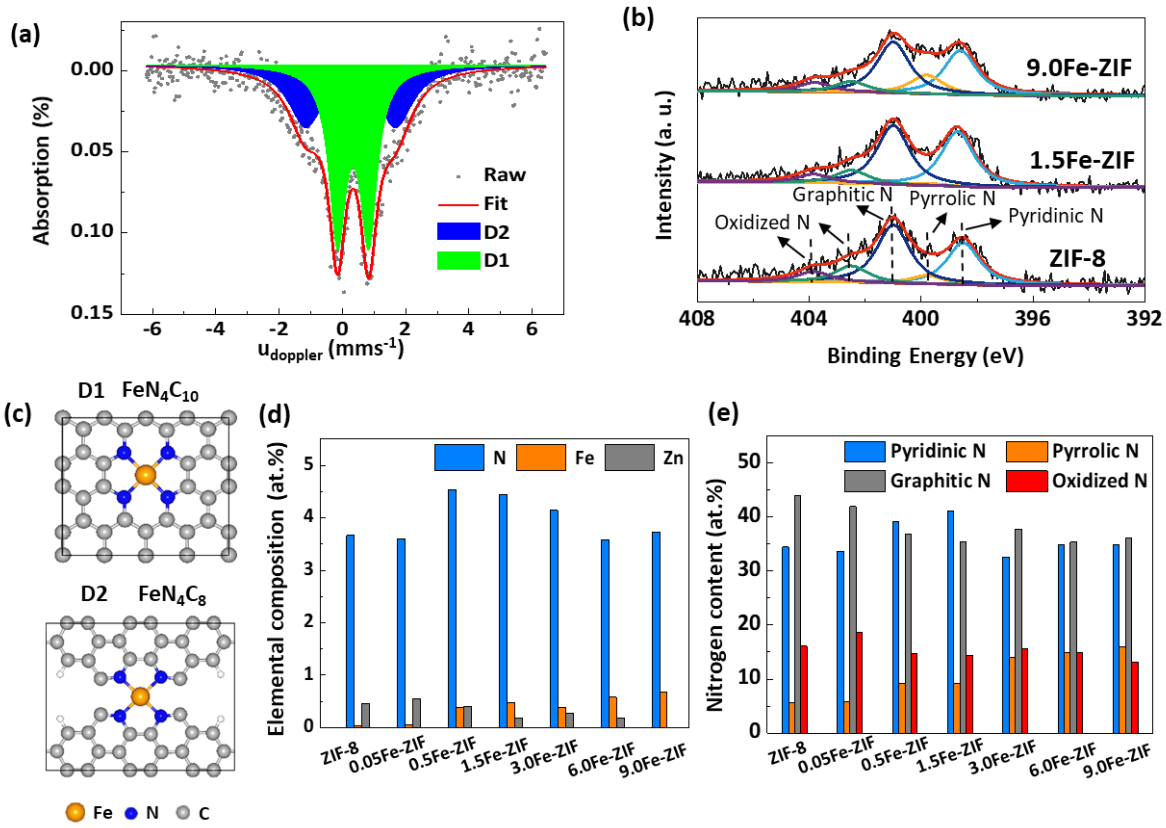

Figure 2. (a) Mößbauer spectroscopy of the best performing atomically dispersed Fe catalyst (1.5Fe-ZIF); (b) The molecule structure of D1 (FeN_4C_{10}) and D2 (FeN_4C_{10}); (c) XPS N1s spectra of ZIF-8, 1.5Fe-ZIF and 9.0 Fe-ZIF catalysts; (d) elemental composition; (e) fraction of various types of nitrogen doping for various Fe-ZIF catalysts as function of Fe doping content in ZIF precursors.

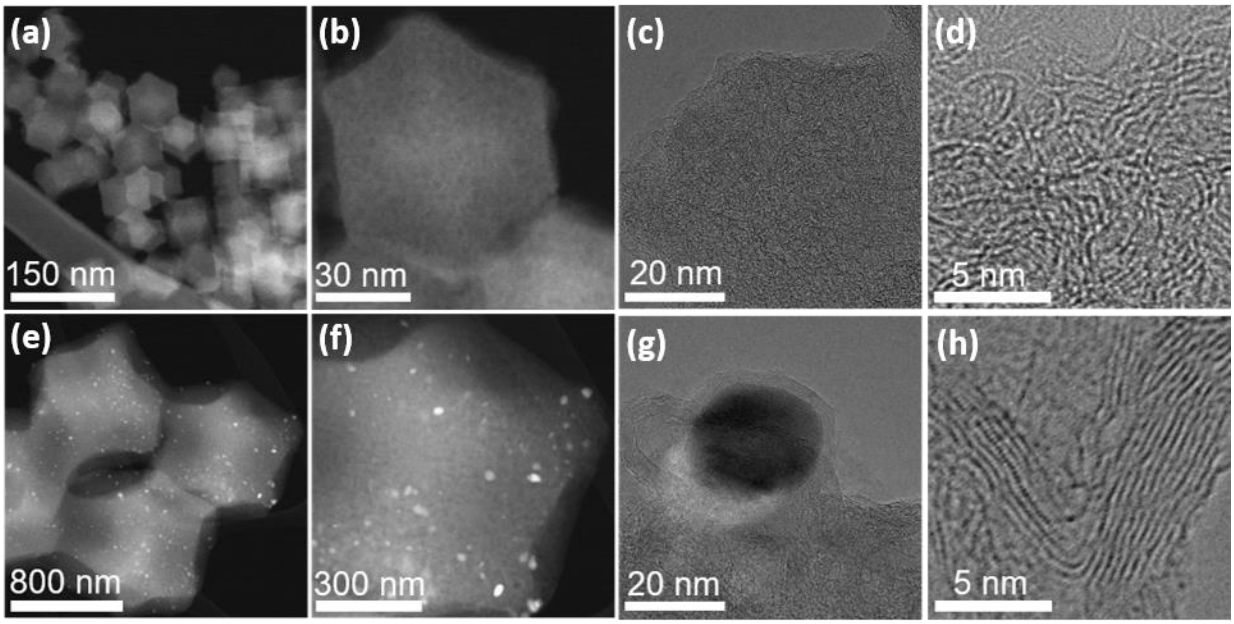

Figure 3. Comparison of catalyst morphology and carbon microstructure in catalysts obtained from Fe-ZIF precursors with (a-d) optimum (1.5 at.%) and (e-h) high (9.0 at.%) Fe content.

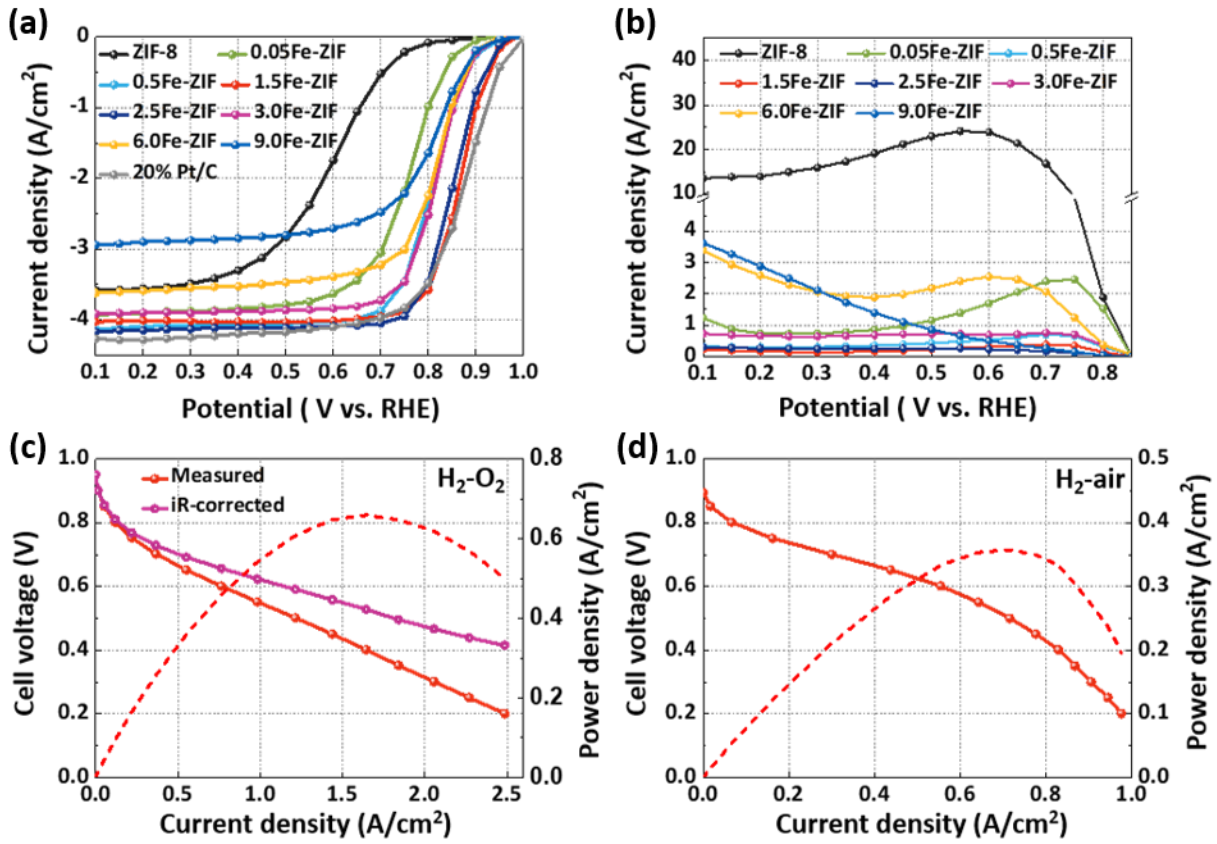

Figure 4. (a) RRDE ORR polarization plots and (b) H_2O_2 yield plots for different Fe-ZIF catalysts as a function of Fe content in the precursor (from 0 to 9 at.%). Test conditions: O_2-saturated 0.5 M H_2SO_4, disk rotation rate 900 rpm, catalyst loading 0.8 mg/cm^2. Fuel cell performance of the 1.5Fe-ZIF catalyst: (c) H_2-O_2 and (d) H_2-air. Anode: 0.2 mg$_{Pt}$/cm^2 Pt/C; H_2 flow rate 200 sccm, 1.0 bar H_2 partial pressure; cathode: *ca.* 4.0 mg/cm^2, 200 sccm gas flow rate, 1.0 bar total partial pressures of gases flown; membrane: Nafion®,211; cell: 80°C, 100% RH, 5.0 cm^2 MEA electrode area.

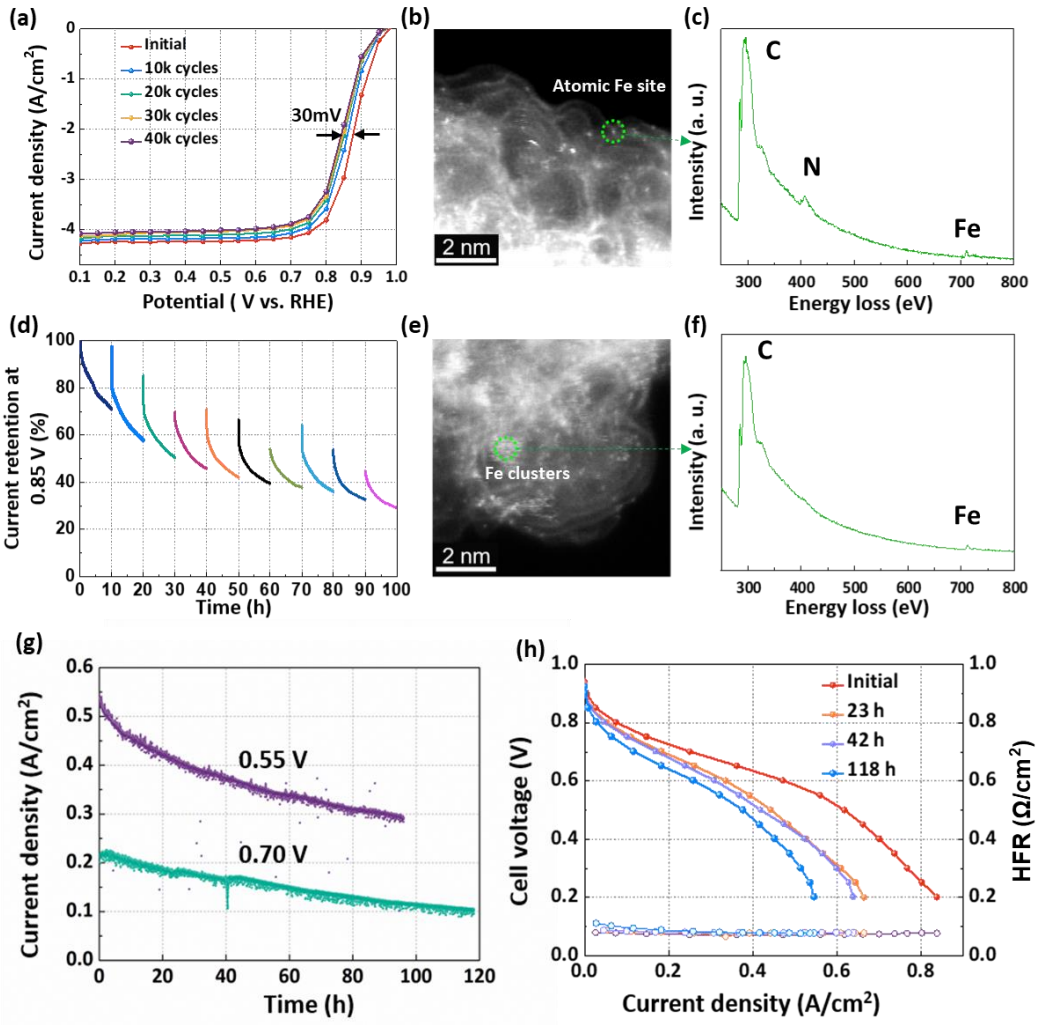

Figure 5. (a, d) RDE stability tests of the best performing 1.5Fe-ZIF catalyst in O_2-saturated 0.5 M H_2SO_4 electrolyte using different test protocols. Structural changes by (b-c) STEM and (e-f) EELS analysis. (a-c) Potential cycling between 0.60 and 1.0 V still showing significant atomically dispersed Fe sites coordinated by N. (d-f) Holding at a constant potential of 0.85 V for 100 hours, significant degradation especially at the initial stage accompanying with depicting appearance of Fe clusters and likely Fe-N bond breaking or weakening. (g) Fuel cell durability tests at a constant potential of 0.70 V and 0.55 V, respectively. (h) Fuel cell polarization plots recorded at different times during the 120-hour durability test at 0.70 V. Fuel cell cathode: catalyst loading 4.0 mg/cm^2; 100% RH; air flown at 200 sccm, 1.0 bar total partial pressure of gases. Anode: Pt/C, 0.20 mg$_{Pt}$/cm^2, 100% RH; H_2 flown at 200 sccm, 1.0 bar partial gas pressure. Membrane: Nafion® 212. Temperature: 80 °C. MEA area: 5.0 cm^2.

Supplementary Information

High-performance fuel cell cathodes exclusively containing atomically dispersed iron active sites

Hanguang Zhang,[a] Hoon T. Chung,[b] David A. Cullen,[c] Stephan Wagner,[d] Ulrike I. Kramm,[d] Karren L. More,[e] Piotr Zelenay,[b,*] and Gang Wu[a,*]

[a] Department of Chemical and Biological Engineering, University at Buffalo, The State University of New York, Buffalo, New York 14260, United States

[b] Materials Physics & Applications Division, Los Alamos National Laboratory, Los Alamos, New Mexico 87545, United States

[c] Materials Science and Technology Division, Oak Ridge National Laboratory, Oak Ridge, Tennessee 37831, United States

[d] Technische Universität Darmstadt, Department of Materials- and Earth Sciences and Department of Chemistry, 64287 Darmstadt, Germany

[e] Center for Nanophase Materials Sciences, Oak Ridge National Laboratory, Oak Ridge, Tennessee 37831, United States

Corresponding authors:

E-mail addresses: gangwu@buffalo.edu (G.W.) and zelenay@lanl.gov (P.Z.)

Figures S1 to S15;

Table S1-S4

Experimental details:

Catalyst synthesis

Fe content is given in this work in terms of atomic percent of Fe versus the total metal (Fe+Zn) content in the synthesis of catalyst precursor from 0.05% to 9.0 at.%. The synthesis of 1.5Fe-ZIF catalyst, i.e., the catalyst derived from precursor with 1.5 at.% Fe content, is given here as an example: Zinc nitrate hexahydrate (3.39 g) and iron nitrate nonahydrate (80 mg) were dissolved in 500 mL methanol in a round-bottom flask, followed by addition of 500 mL methanol solution of 2-methylimidazole (3.94 g). The obtained mixture were then kept at 60 °C for 24 h. The resulting suspension was separated by centrifuging at 8700 rpm to collect the precipitants, then washed with ethanol three times. The thus obtained catalyst precursor was dried at 60 °C in a vacuum oven for 8 h, before being heat-treated in a tube furnace at 1100 °C under N_2 for 1 h to obtain final catalyst (1.5Fe-ZIF in this example). The ZIF-8 derived Fe-free catalyst follows the same synthetic procedure above except for the addition of iron nitrate nonahydrate.

Material characterization

Atomic-resolution micrographs were obtained using a Nion UltraSTEM U100 microscope operated at 60 keV and equipped with a Gatan Enfina electron energy loss spectrometer (EELS). Bright field (BF) and high-angle annular dark-field (HAADF) micrographs were recorded in image pairs. EEL spectra to confirm the composition of Fe sites and clusters were obtained after eliminating data noise using the open source Hyperspy python library. Catalyst morphology was also studied using scanning electron microscopy (SEM) on a Hitachi SU 70 microscope operating at 5 kV. The crystal phases in the samples were identified using powder X-ray diffraction (XRD) on a Rigaku Ultima IV diffractometer with Cu K-α X-rays. X-ray photoelectron spectroscopy (XPS) was performed using a Kratos AXIS Ultra DLD XPS system equipped with a hemispherical energy analyzer and a monochromatic Al Kα source. The high-resolution of N1s spectra were fitted with four types of N bonding, including pyridinic N (398.6 eV), pyrrolic N (399.6 eV), graphitic N (401.1 eV) and oxidized N (402.6 eV and 403.8 eV). The elemental Fe content in precursors was determined by inductively coupled plasma (ICP), after complete digestion of precursors in 65% nitric acid. The N_2 isothermal adsorption/desorption was recorded at 77 K using a Micromeritics TriStar II BET instrument. Samples were degassed at 150 °C for 5 h under vacuum prior to nitrogen physisorption measurements. Mößbauer spectroscopy was performed in transmission mode at room temperature using a Co^{57}/Rh source. Data were collected with a scintillation detector and calibration of the velocity axis was made with respect to α–Fe foil. The Raman spectra of catalysts coated on glass slides were recorded with a wavelength of 514 nm laser at ambient condition by the Renishaw Raman system.

Electrochemical measurements

All electrochemical measurements were performed using a CHI Electrochemical Station (Model 760b) in a conventional three-electrode cell at room temperature. A glassy carbon rotating disk electrode (GC-RDE) was used as the working electrode. Each catalyst was mixed with isopropanol and 5 wt% suspension of Nafion® in alcohols to produce catalyst ink that was drop-cast onto the GC-RDE and air-dried at 60 °C. Cyclic voltammetry (CV) was then recorded in N_2-saturated 0.5 M H_2SO_4 electrolyte at a scan rate of 20 mV/s to

estimate the electrochemically accessible surface area from the double layer capacitance, assuming a capacitance 30 μF per cm^2 of the catalyst surface (These M-N-C catalysts contain almost 95% of carbon.), following the approach in our previous work[52]. The ORR activity and four-electron selectivity were determined from rotating ring disc electrode (RRDE) measurements, performed in O_2-saturated 0.5 M H_2SO_4 at room temperature and rotation rate of 900 rpm. A graphite rod was used as the counter electrode. $Hg/HgSO_4$ in saturated K_2SO_4, was the reference electrode. The catalyst loading RDE/RRDE testing was 0.8 mg/cm^2, except in the loading dependence studies. ORR steady-state polarization plots were recorded using potential steps of 0.05 V at time intervals of 30 s in the potential range from 1.0 to 0 V *vs*. RHE. The potential of platinum ring on RRDE was kept at 1.2 V *vs*. RHE during recording ORR polarization curves. The hydrogen peroxide yield was calculated from the recorded ring (I_r) and disk current (I_d) using the following equation where N=0.36 is collection efficiency:

$$H_2O_2 \text{ yield } (\%) = 200I_r/(I_r+NI_d)$$

Two accelerated stress testing approaches (potential cycling and constant potential holding) are both employed to evaluate the stability of catalysts in RRDE. The potential cycling was carried out from 0.6 to 1.0 V *vs*. RHE for 40,000 cycles in an oxygen saturated 0.5 M H_2SO_4. The polarization curves were recorded every 10,000 cycles. Chronoamperometry was used to conduct constant potential holding at 0.85 V *vs*. RHE for 100 h in an oxygen saturated 0.5 M H_2SO_4. The corresponding polarization curves were taken every 10 h.

Fuel cell testing

Catalyst ink containing 35 wt% of Nafion® was made by ultrasonically mixing the catalyst, isopropanol, de-ionized water, and 5% Nafion® suspension in alcohols at a 1:12:12:11 weight ratio for three hours. The inks were applied to the membrane by brushing until the cathode catalyst loading of ~4.0 mg cm^{-2} was reached. A commercial Pt-catalyzed gas diffusion electrode (GDE, 0.2 mg_{Pt}/cm^2, IRD Fuel Cells) was used at the anode. The cathode gas diffusion layer and the anode GDE were hot-pressed onto a Nafion® 212/211 membrane at 125°C for 5 minutes. The geometric surface area of the membrane electrode assembly (MEA) was 5.0 cm^2. Fuel cell testing was carried out in a single-cell fuel cell with a single-serpentine flow channels. Pure hydrogen and air/oxygen humidified at 80 °C were supplied to the anode and cathode, respectively, at a flow rate of 200 mL/min. The total partial pressure of gases at both electrodes was 1.0 bar. Fuel cell polarization plots were recorded using standard fuel cell test stations (Fuel Cell Technologies Inc.) in a voltage control mode. Chronoamperometry was employed to record the current change during the constant potential holding at 0.7 V or 0.55 V for 118 h and 95 h in the H_2-air cell with the same condition used for testing polarization curves.

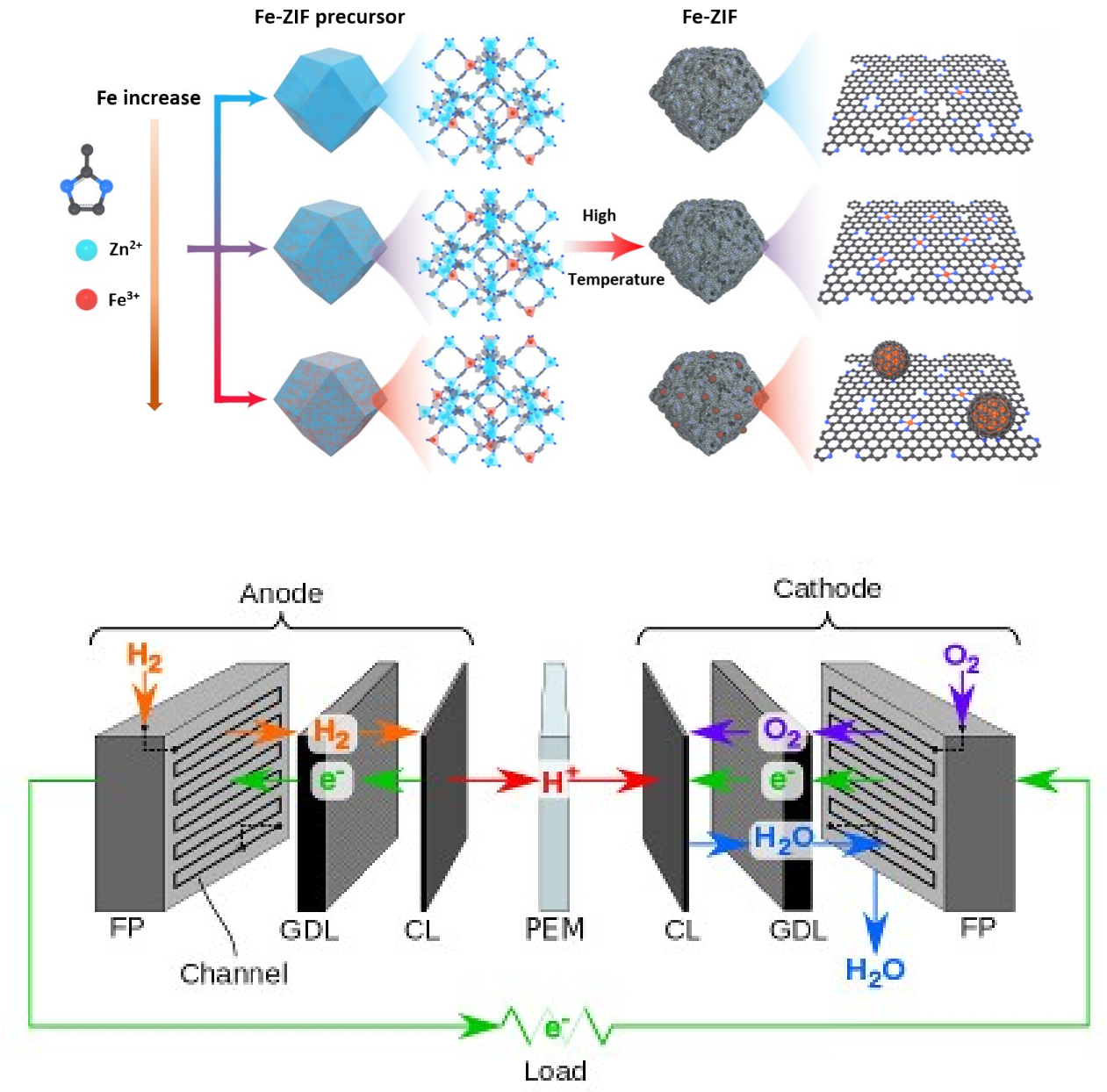

Figure S1. (*Top*) Schematic illustration of synthesis of precursor Fe-ZIF and their derived catalysts Fe-ZIF with various doped Fe content in ZIF-8 precursors. (*Bottom*) Basic An assembled fuel cell hardware used for PEFC tests (*Reproduced from fuel cell training materials of Los Alamos National Laboratory*)

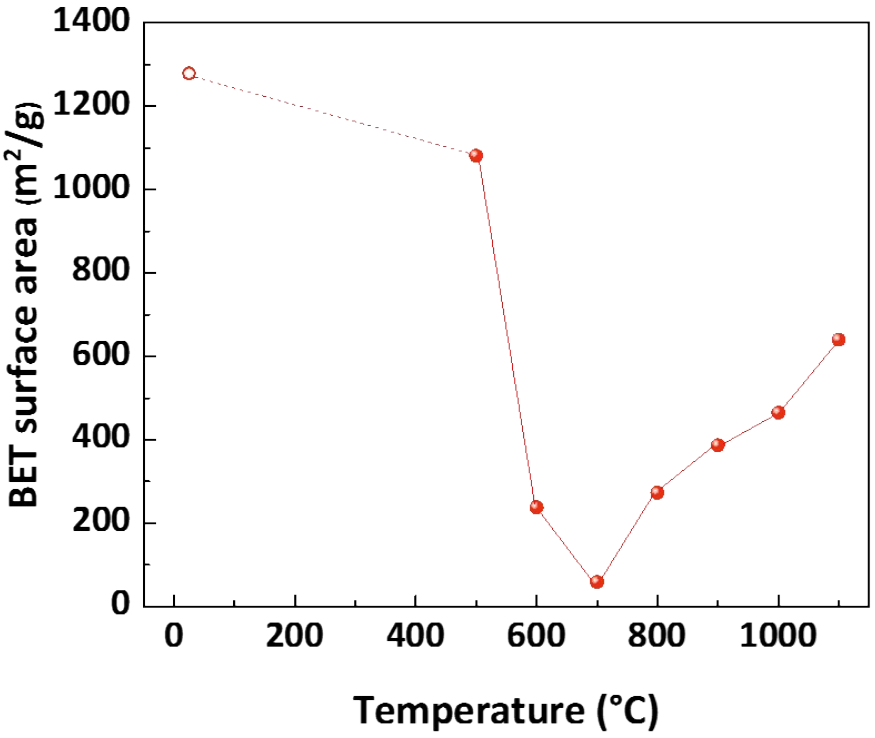

Figure S2. The BET surface area of 1.5Fe-ZIF as a function of the heat-treatment temperature in the range from 500 °C to 1100 °C. The BET surface area of the precursor is shown with an open circle.

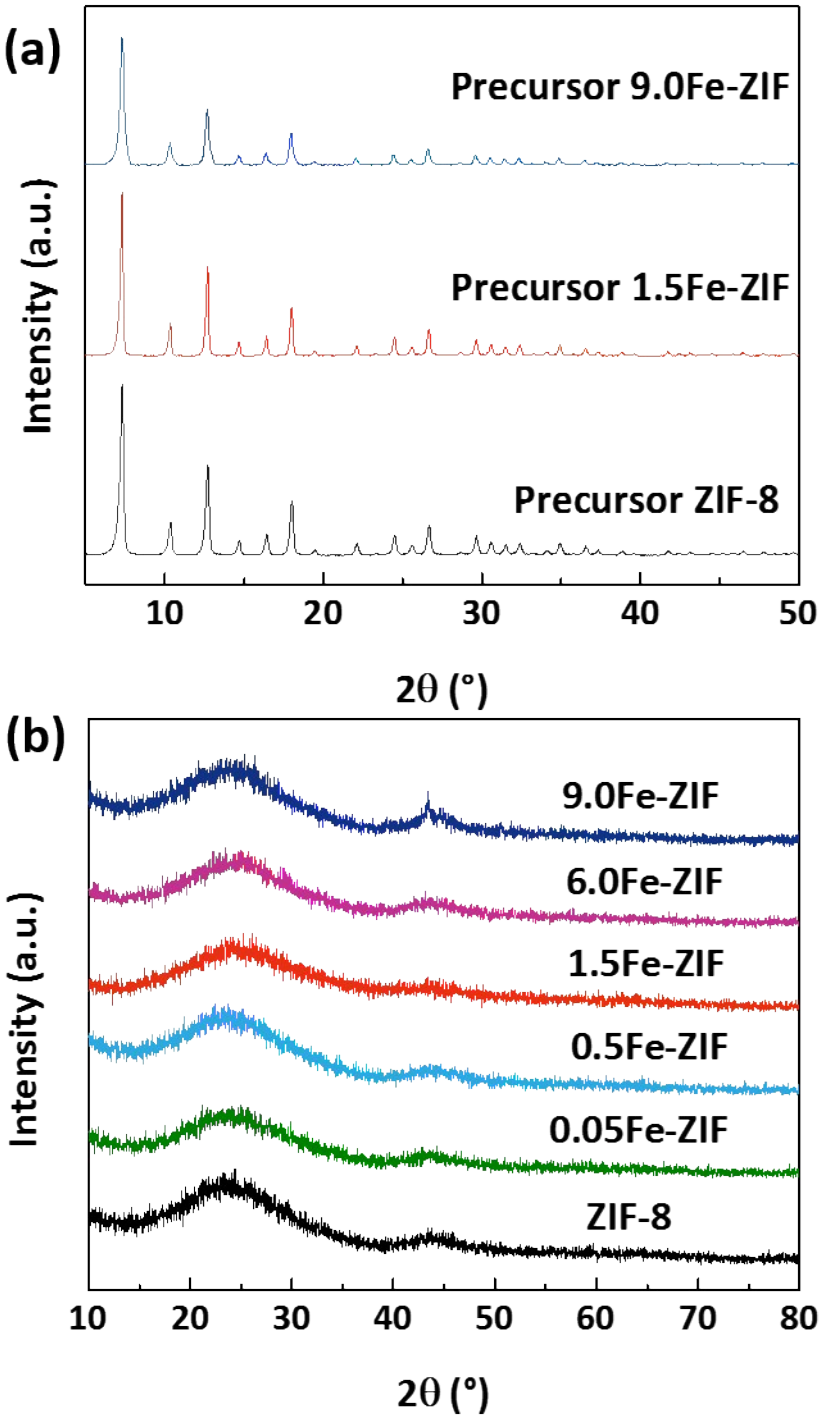

Figure S3. XRD patterns for **(a)** Fe-free and Fe-doped ZIF precursors and **(b)** ORR catalysts obtained after single heat-treatment at 1100 °C as a function of the doped Fe content.

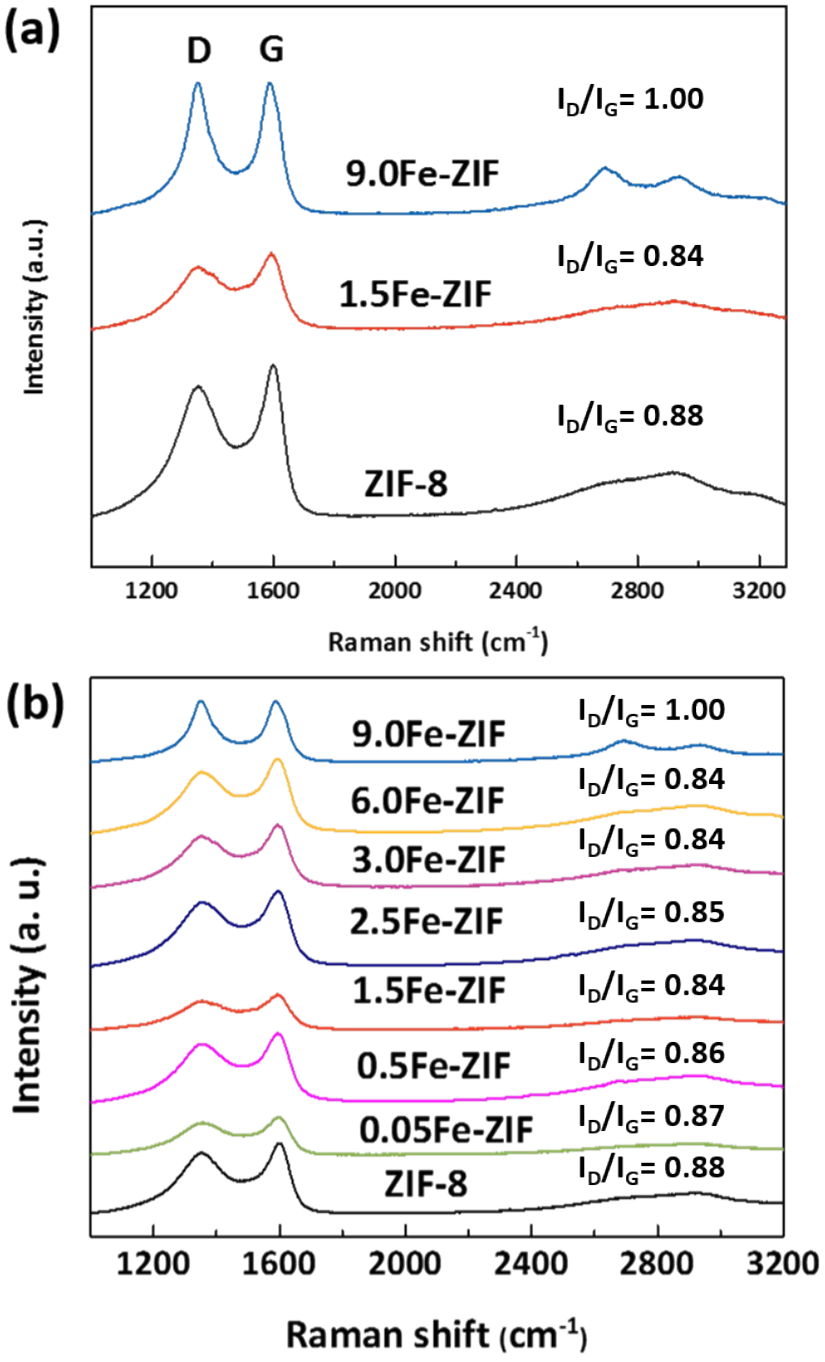

Figure S4. Raman spectroscopy of the Fe-ZIF catalysts (pyrolyzed at 1100 °C) with different Fe content in the precursor. **(a)** Raman spectra for three selected catalysts (Fe-free and two Fe-containing ones); **(b)** Raman spectra for all studied catalysts.

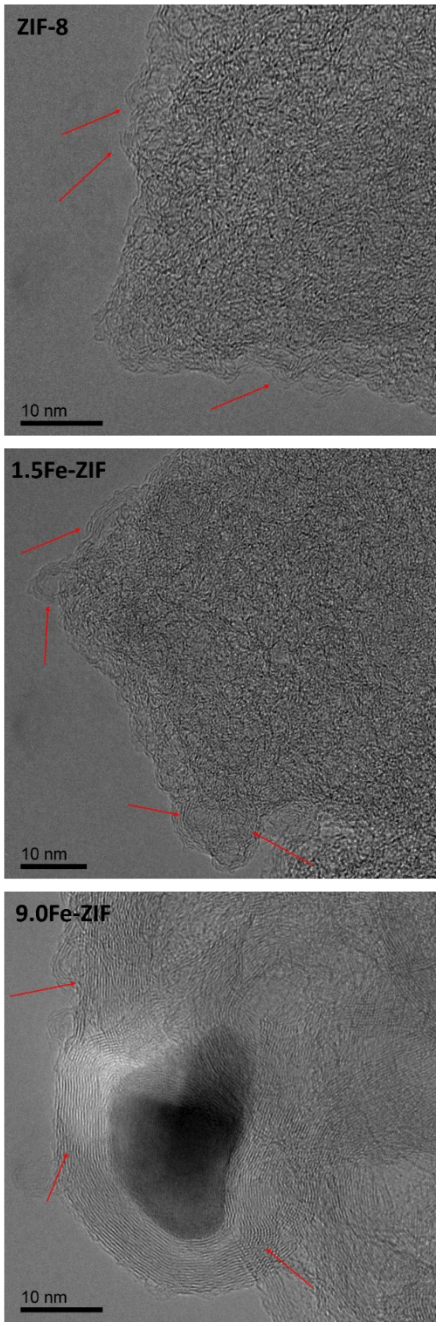

Figure S5. The HR-TEM images of the carbon structure of catalysts derived from ZIF-8; 1.5Fe-ZIF, and 9.0Fe-ZIF. Red arrows pointing to different carbon structures present.

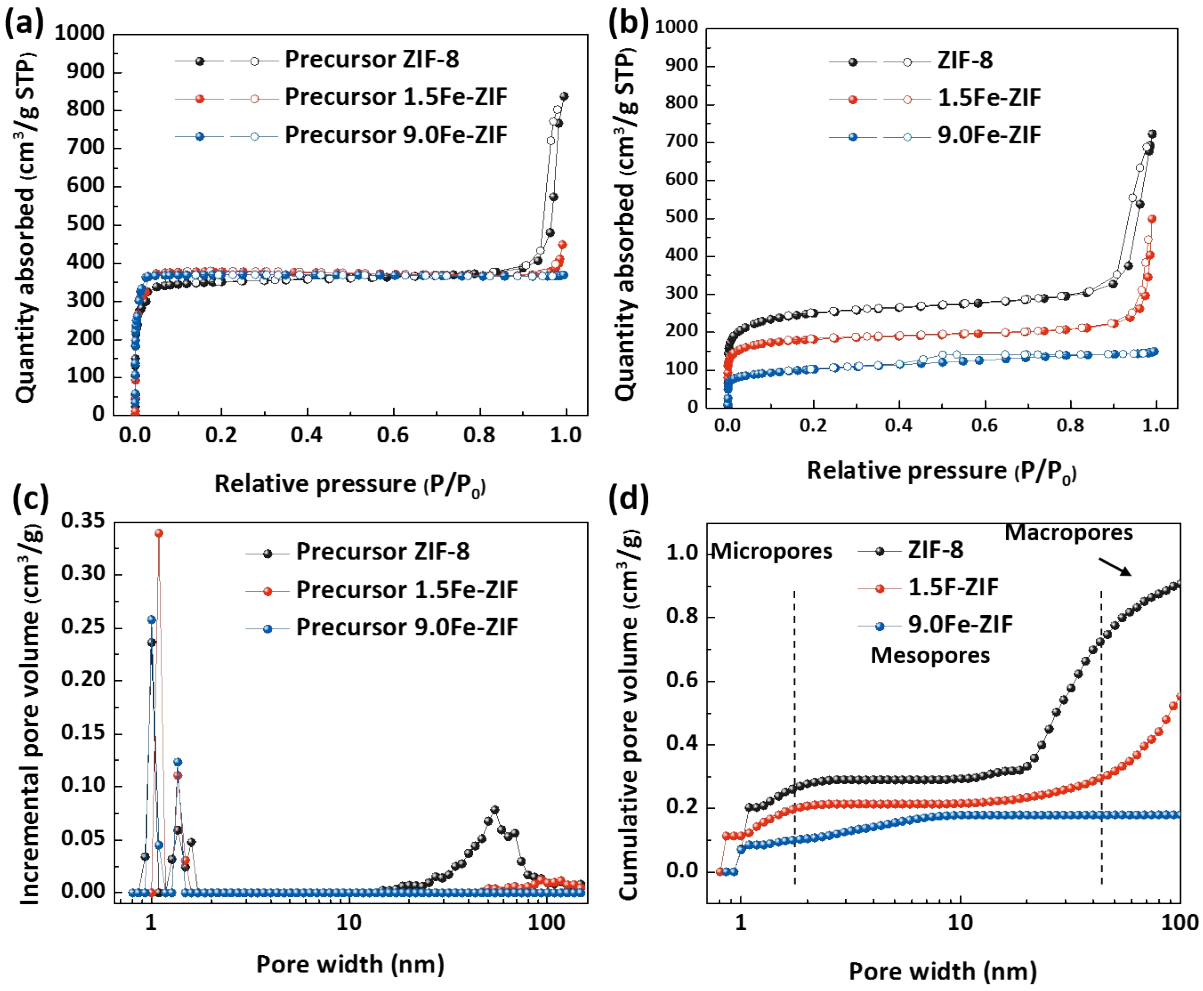

Figure S6. Isothermal N_2 sorption curves for **(a)** ZIF-8, 1.5Fe-ZIF and 9.0Fe-ZIF precursors and **(b)** catalysts derived from these precursors. **(c)** Pore-size distribution plots for ZIF-8, 1.5Fe-ZIF and 9.0Fe-ZIF precursors; **(d)** cumulative pore volume in ZIF-8, 1.5Fe-ZIF and 9.0Fe-ZIF catalysts as a function of the pore width.

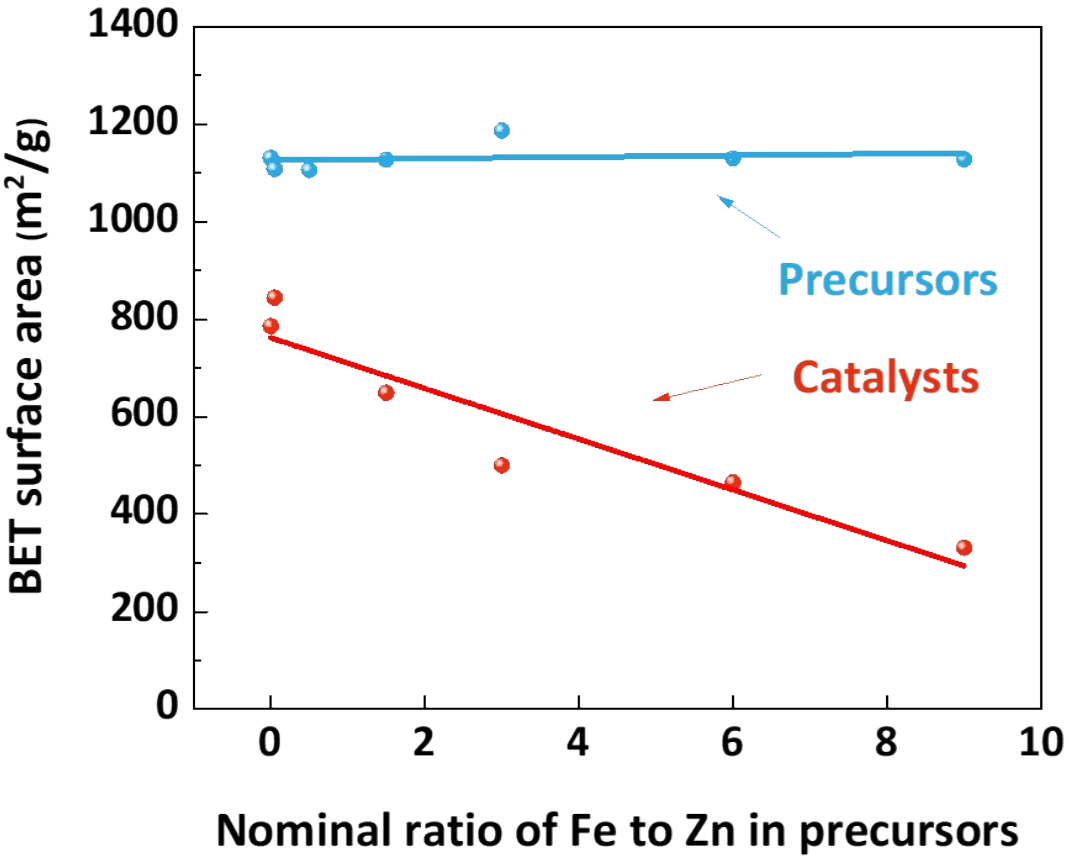

Figure S7. BET surface area of the Fe-doped ZIF precursors and catalysts derived from these precursors as a function of the doped Fe content.

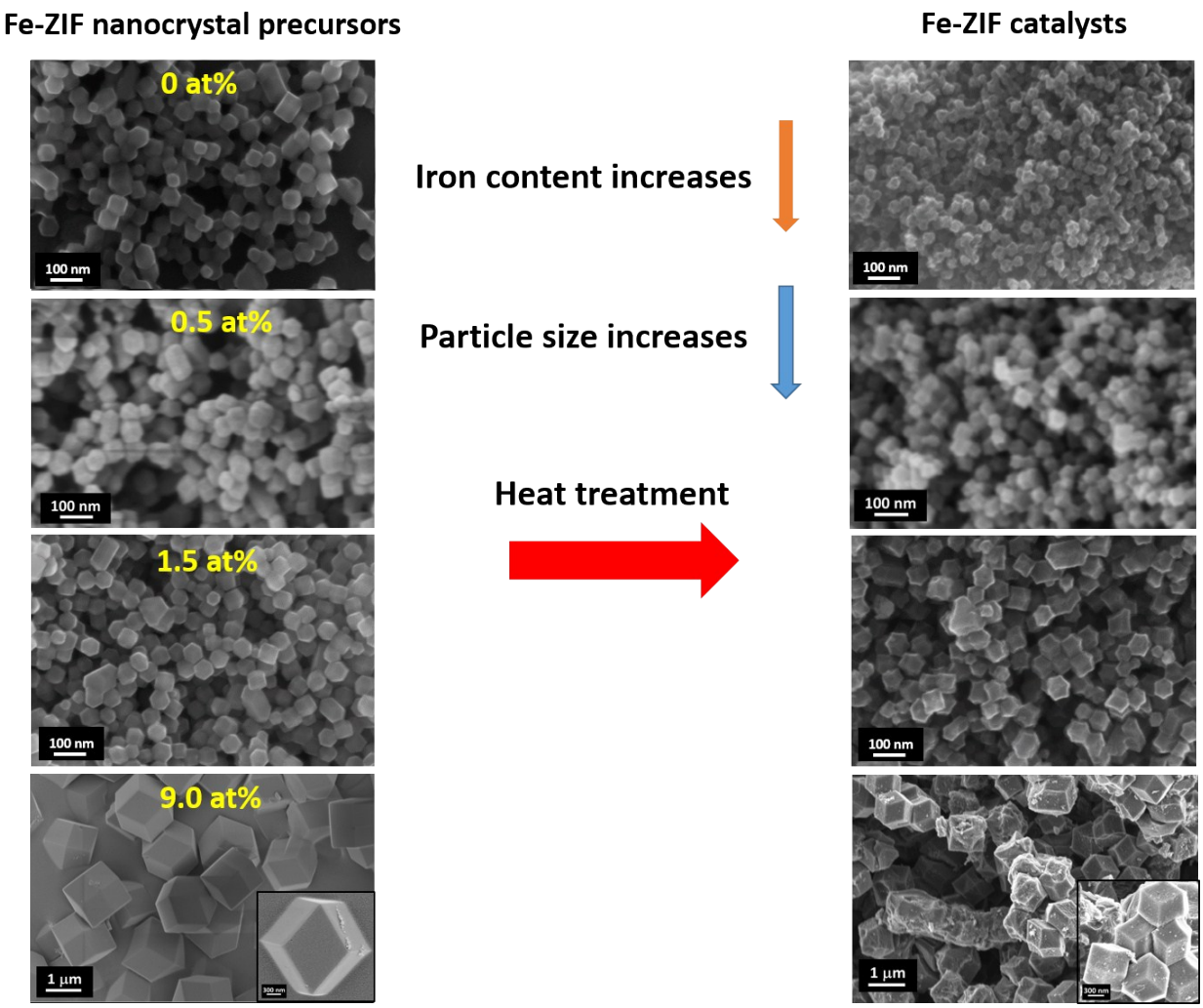

Figure S8. Scanning electron microscopy images of Fe-doped ZIF precursors with various Fe content (left) and of the corresponding catalysts after the heat treatment at 1100 °C (right).

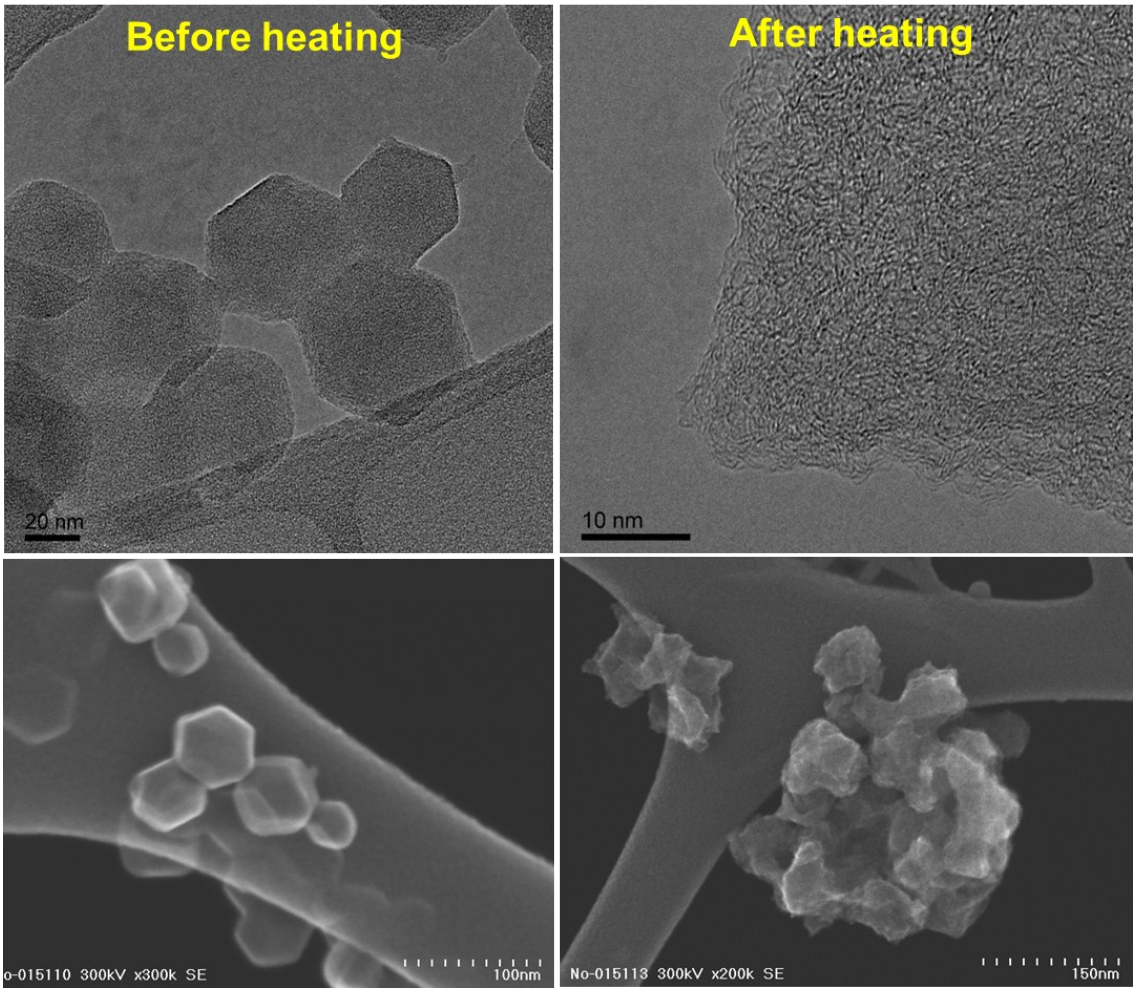

Figure S9. Morphology of the "Fe-free" ZIF-8 precursor and catalyst before and after the heat treatment at 1100 °C.

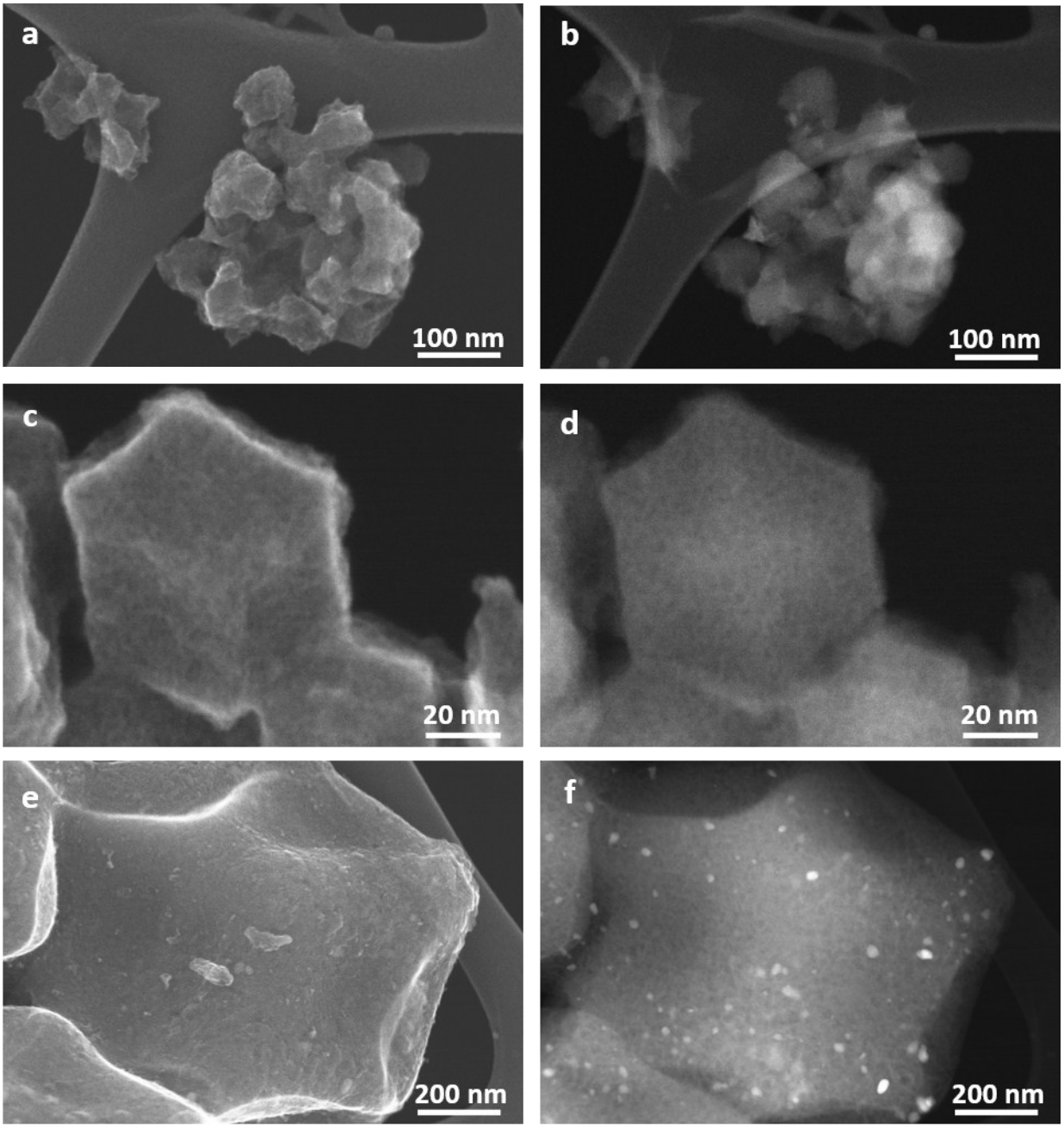

Figure S10. TEM images in bright field mode and in HAADF mode for catalysts derived from **(a, b)** ZIF-8, **(c, d)** 1.5Fe-ZIF, and **(e, f)** 9.0Fe-ZIF.

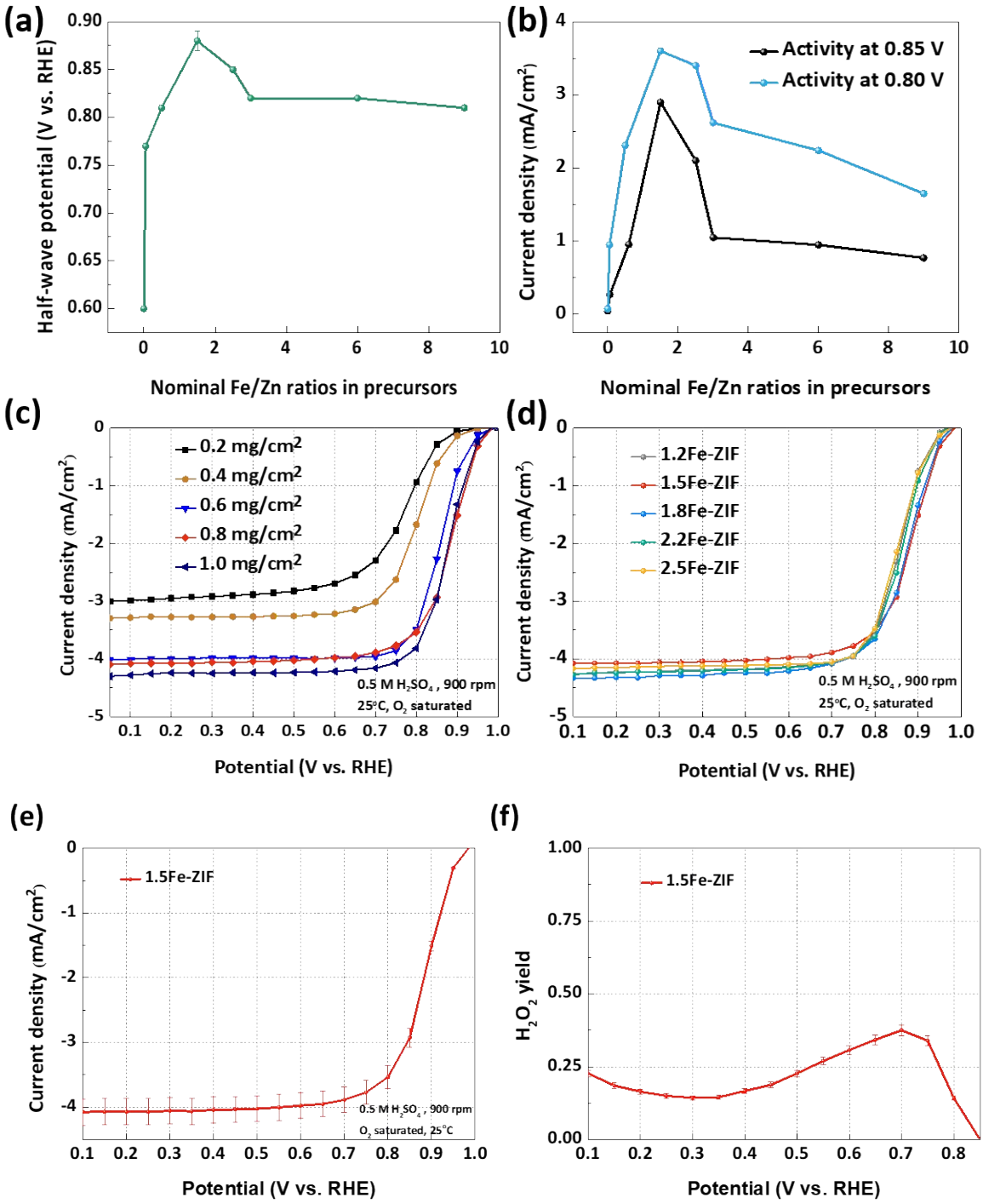

Figure S11. ORR activity of Fe-ZIF catalysts as a function of the doped-Fe content using **(a)** ORR half-wave potential determined in RDE testing at a rotation speed of 900 rpm and **(b)** current density at high potentials of 0.85 V and 0.80 V; catalyst loading of 0.8 mg/cm^2. **(c)** ORR RDE plots for the best performing 1.5Fe-ZIF catalyst at different loadings at the disk. **(d)** ORR RDE plots for Fe-ZIF catalysts with Fe content from 1.2 to 2.5 at%. ORR activity (**e**) and selectivity **(f)** for the best performing Fe-N-C catalysts with error bars.

Table S1. Summary of RDE performance in acidic electrolytes of the most active 1.5Fe-ZIF catalyst in this work and several Fe-N-C catalysts reported in literature.

Catalyst	Electrolyte and disk rotation rate/rpm	Onset potential/V (*vs.* RHE)	Half-wave potential /V (*vs.* RHE)	Current density at 0.9 V (*vs.* RHE) /mA cm^{-2}	Ref.
1.5Fe-ZIF	0.5 M H_2SO_4, 900	0.98	0.88	1.5	This work
$Fe_{0.5}$-900	0.1 M H_2SO_4, 1600	0.99	0.88	1.5	1
$Zn(eIm)_2TPIP$	0.1 M $HClO_4$, 1600	0.91	0.78	0.1	2
Fe/N/C/NF	0.5 M H_2SO_4, 900	0.93	0.80	0.2	3
Fe SAs/N-C	0.1 M $HClO_4$, 1600	0.95	0.75	0.4	4
PAN-Fe-C	0.5 M H_2SO_4, 900	0.93	0.80	0.2	5
(CM+PANI) Fe-C	0.5 M H_2SO_4, 900	0.95	0.80	0.2	6
Fe-N-C	0.1 M $HClO_4$, 1600	0.94	0.84	0.8	7
Fe-PAN-EN-hydrogel	0.5 M H_2SO_4, 900	0.95	0.83	0.8	8
(DFTPP)Fe-Im-CNTS	0.1 M $HClO_4$, 1600	1.05	0.88	2.5	9
pCNT@Fe1.5%@GL-NH_3	0.1 M $HClO_4$, 1600	0.98	0.88	2.0	10

Table S2. Summary of calculation for the maximum mass-based site density, mass-based kinetic current and turnover frequency

Catalysts	Fe /wt%	Fe (D1) /wt%	MSD_{max} /site g_{cat}^{-1}	I_{kin} (0.8 V) /A g_{cat}^{-1}	TOF (0.8 V) /e $s^{-1}site^{-1}$	Ref
1.5Fe-ZIF	2.14[a]	1.24	1.34×10^{20}	45.0	2.14	This work
FePhenMOF-$ArNH_3$	0.5[b]	0.2	2.16×10^{19}	7.78	2.40	12
Fe-N-C-3HT-2AL	6.0[b]	1.33	1.43×10^{20}	21.0	0.92	7

a determined by XPS
b determined by ICP

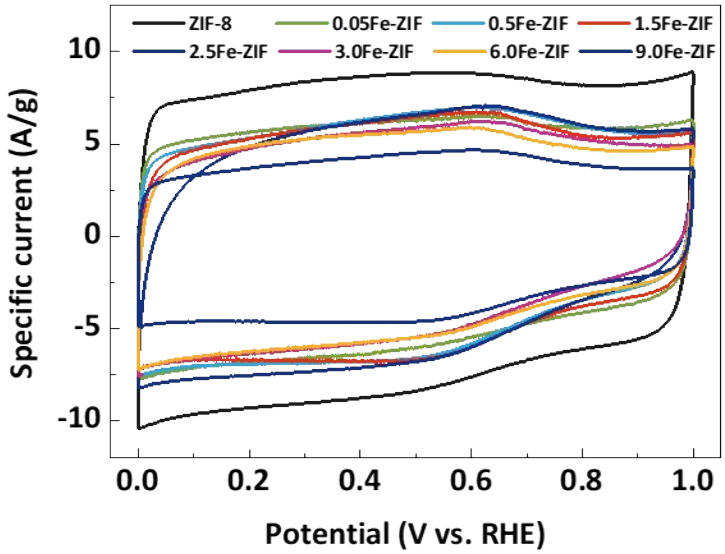

Figure S12. Cyclic voltammetry of Fe-free and Fe-ZIF catalysts in N_2 saturated 0.5 M H_2SO_4

Table S3. Electrochemically accessible surface area of Fe-free and Fe-ZIF-derived catalysts.

Catalysts	Electrochemically accessible surface area (m^2/g)
ZIF-8	795
0.05Fe-ZIF	570
0.5Fe-ZIF	566
1.5Fe-ZIF	556
2.5Fe-ZIF	554
3.0Fe-ZIF	495
6.0Fe-ZIF	488
9.0Fe-ZIF	388

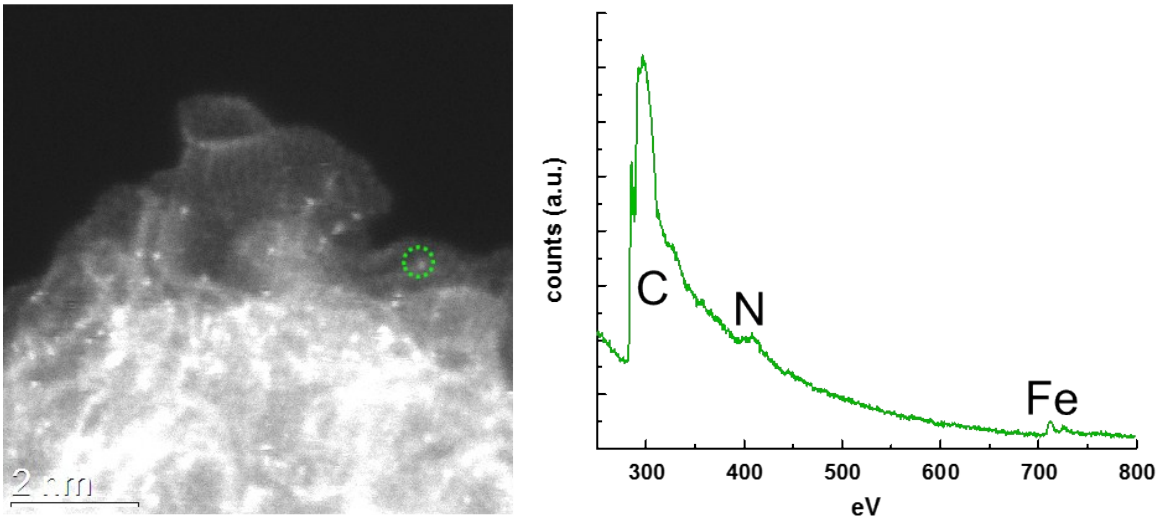

Figure S13. The HAADF-STEM image of the 1.5Fe-ZIF catalyst after the cycling stability test and the electron energy loss (EEL) spectra from the specified point cycled in green.

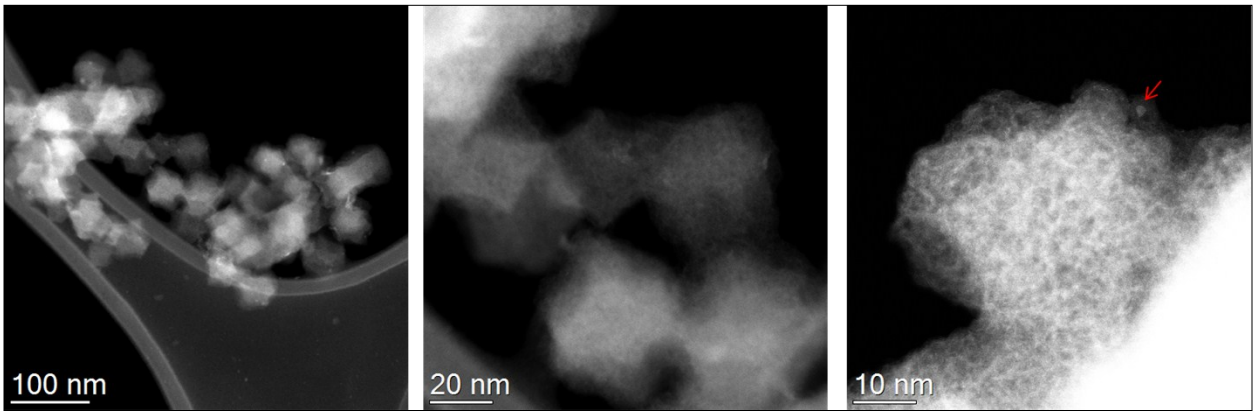

Figure S14. Carbon particle morphology in 1.5Fe-ZIF catalysts after potential cycling from 0.6 to 1.0 V in O_2-saturated 0.5 M H_2SO_4 solution for 30,000 cycles.

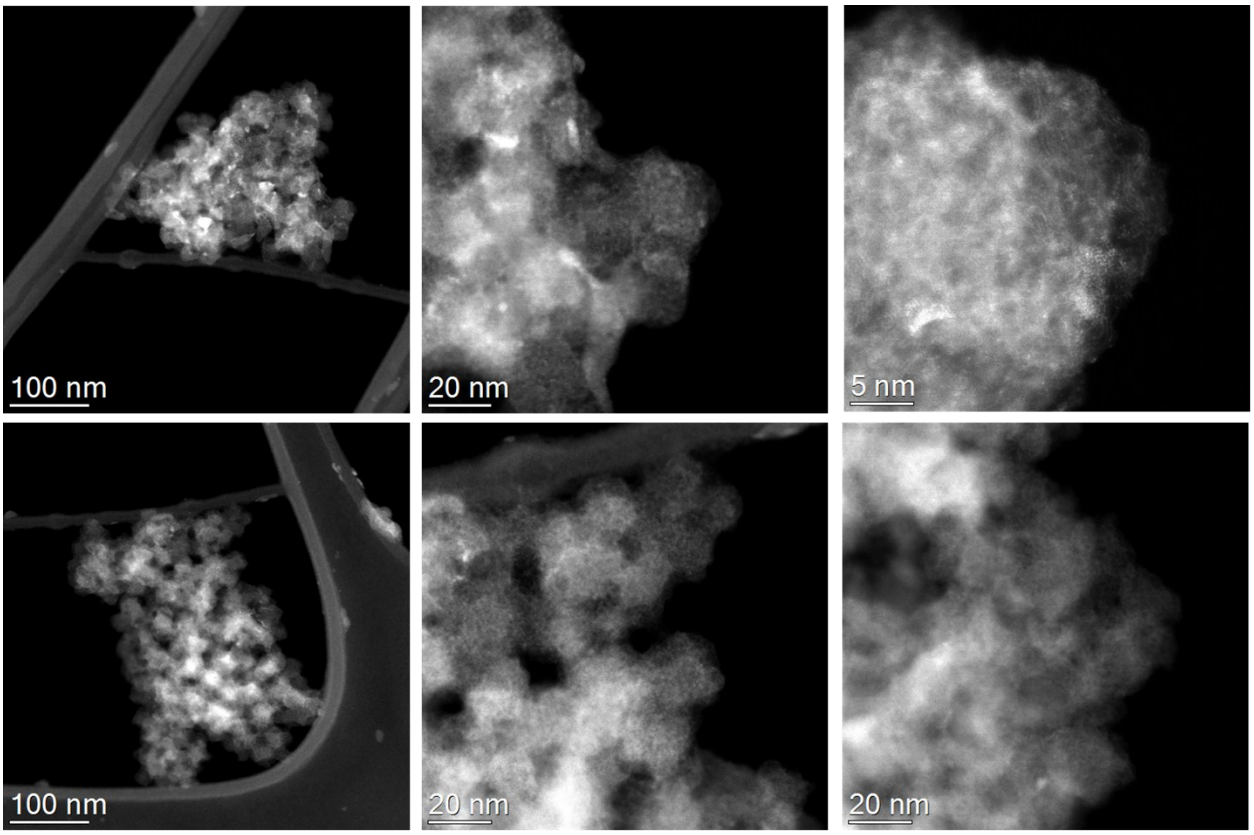

Figure S15. Carbon particle morphology of the 1.5Fe-ZIF catalyst after the durability test at a constant potential of 0.85 V for 100 hours. Micrographs highlight the appearance of Fe clusters and rounding of the carbon particles that implies carbon corrosion.

Table S4. Summary of activity and durability for PGM-free catalysts at RDE and fuel cells

Catalysts	Times of heat treatment	Acid-leaching	RDE tests in acid electrolyte		MEA tests				Ref.
			Activity	Stability	Activity		Durability		
			$E_{1/2}$ /V vs. RHE	Loss in $E_{1/2}$ /V vs. RHE (cycle numbers from 0.6-1.0 V vs. RHE)	Current density @0.8 V /mA and ($P_{oxidant}$)	Peak power density /W	Current retention /%, testing voltage /V, and duration /h	Power density[d] /W, (testing voltage /V, and duration/h)	
1.5Fe-ZIF	1	No	0.88	20 mV (10,000 cycles) 30 mV (40,000 cycles)	75[b] (1 bar); 120[c] (1 bar)	0.36[b] 0.67[c]	48[b] (0.7 V, 118 h) 51[b] (0.55 V, 95 h)	0.15[b] (0.55 V, 95 h)	This work
$Fe_{0.5}$-950	2	No	0.88	-	150[c] (1.5bar)	-	46[c] (0.5 V, 50 h)	0.25[c] (0.5 V 50 h)	1
1/20/80-Z8-1050°C-15	2	No	-	-	400[c] (1.5 bar)	0.91[c]	43[b] (0.5 V, 100h) 22[c] (0.5 V 100h)	0.13[b] (0.5 V 100 h) 0.11[c] (0.5 V 20 h)	11
Fe/N/CF	3	Yes	0.80	8 mV (35,000 cycles)[a]	250[c] (2 bar)	0.90[c]	28[c] (0.5 V,100h)	0.14[c] (0.5 V, 100h)	3
FePhen MOF–$ArNH_3$	2	Yes	0.78	-	50[b] (2.5 bar)	0.40[b]	-	-	12
SA-Fe/NG	1	Yes	0.80	8m V (5,000 cycles)	100[c] (2.5 bar)	0.82[c]	23[c] (0.5 V, 20 h)	0.13[c] (0.5 V, 20h)	13
pCNT @Fe1.5%@GL-NH_3	3	No	0.88	80 mV (10,000 cycles)	-	-	-	-	10

a Stability test in N_2 saturated acids. Other catalysts were tested in O_2 saturated acids.

b H_2-air cell

c H_2-O_2 cell

d Calculated power density at the voltage for durability test

References

1 A. Zitolo, V. Goellner, V. Armel, M.-T. Sougrati, T. Mineva, L. Stievano, E. Fonda and F. Jaouen, Nature Materials, 14, 937.

2. D. Zhao, J.-L. Shui, L. R. Grabstanowicz, C. Chen, S. M. Commet, T. Xu, J. Lu and D.-J. Liu, Advanced Materials, 2014, 26, 1093-1097.

3. J. Shui, C. Chen, L. Grabstanowicz, D. Zhao and D. J. Liu, Proceedings of the National Academy of Sciences of the United States of America, 2015, 112, 10629-10634.

4. J. Wang, Z. Huang, W. Liu, C. Chang, H. Tang, Z. Li, W. Chen, C. Jia, T. Yao, S. Wei, Y. Wu and Y. Li, Journal of the American Chemical Society, 2017, DOI: 10.1021/jacs.7b10385.

5. G. Wu, K. L. More, C. M. Johnston and P. Zelenay, Science, 2011, 332, 443-447.

6. H. T. Chung, D. A. Cullen, D. Higgins, B. T. Sneed, E. F. Holby, K. L. More and P. Zelenay, Science, 2017, 357, 479-484.

7. N. R. Sahraie, U. I. Kramm, J. Steinberg, Y. Zhang, A. Thomas, T. Reier, J.-P. Paraknowitsch and P. Strasser, Nature Communications, 2015, 6.

8. Z. Qiao, H. Zhang, S. Karakalos, S. Hwang, J. Xue, M. Chen, D. Su and G. Wu, Applied Catalysis B: Environmental, 2017, 219, 629-639.

9. W. Ping-Jie, Y. Guo-Qiang, N. Yoshinori and L. Jin-Gang, Angewandte Chemie International Edition, 2014, 53, 6659-6663.

10. S. H. Ahn, X. Yu and A. Manthiram, Advanced Materials, 2017, 29, 1606534.

11. Proietti, E.; Jaouen, F.; Lefèvre, M.; Larouche, N.; Tian, J.; Herranz, J.; Dodelet, J.-P. Nat Commun 2011, 2, 416.

12. Li, J.; Ghoshal, S.; Liang, W.; Sougrati, M.-T.; Jaouen, F.; Halevi, B.; McKinney, S.; McCool, G.; Ma, C.; Yuan, X.; Ma, Z.-F.; Mukerjee, S.; Jia, Q. *Energ. Envi. Sci.* 2016, *9*, 2418.

13. Yang, L.; Cheng, D.; Xu, H.; Zeng, X.; Wan, X.; Shui, J.; Xiang, Z.; Cao, D. Proceedings of the National Academy of Sciences 2018, 115, 6626.